RSC Advances

PAPER

View Article Online
View Journal | View Issue

Cite this: *RSC Adv.*, 2026, **16**, 25402

Green synthesis of TiO_2/Ag@*Eucalyptus globulus* Labill nanocomposites: a comprehensive study and dual application in grape preservation and dye treatment

Ngoc Linh Nguyen,[a] Hoang Thai,[bc] Thi Thuy Dung Nguyen,[d] Tran Dung Hoang,[b] Dang Hoang Nguyen[e] and Thuy Chinh Nguyen *[bc]

This study presents the green synthesis of TiO_2/Ag@*Eucalyptus globulus* Labill (TiAgxPE) nanocomposites and their integration into chitosan (CS) active packaging films. Distinct from conventional chemically synthesized TiO_2/Ag and those utilizing standard plant extracts, the *Eucalyptus* extract provides unique phytochemicals that act as highly efficient reducing agents while imparting a synergistic capping layer. XRD analysis results confirmed nano TiO_2 formed in the anatase phase, with crystallite sizes increasing from 12.77 nm (TiPE) to 14.88 nm (TiAg0.33PE). UV-vis DRS revealed a narrowed bandgap induced by Ag surface plasmon resonance, while PL peaks at 510–520 nm indicated significantly suppressed electron–hole recombination. HR-TEM images and EDX mapping showed uniformly dispersed face-centered cubic Ag nanoparticles on porous TiO_2. Consequently, the TiAg0.33PE nanocomposite exhibited superior photocatalysis, nearly fully degrading RGB dye in 30 minutes at pH 4. Mechanistic studies revealed that superoxide radicals and photogenerated holes dominated the degradation process, facilitated by efficient unidirectional charge separation at the Ag–TiO_2 Schottky barrier. Furthermore, the TiAg1PE nanoparticles exhibited broad-spectrum antibacterial activity, effectively inhibiting *E. coli*, *S. aureus*, *B. cereus*, and *P. stutzeri B27*, yielding maximum inhibition zones of 12 mm. Incorporating these nanoparticles into CS films reduced the water vapor transmission rate by creating a tortuous diffusion path. Although mechanical flexibility slightly decreased, the CS + TiAg1PE film retained excellent bactericidal efficacy. Over a 9-day storage period, the CS + TiAg1PE formulation reduced moisture loss and microbial decay, limiting weight loss to 15% and confining decay incidence to 5%. Ultimately, these findings underscore the potential of the green synthesized TiAgxPE nanocomposites as a dual-functional platform for photocatalytic wastewater treatment and postharvest shelf-life extension of fresh agricultural produce.

Received 27th February 2026
Accepted 5th May 2026

DOI: 10.1039/d6ra01730d

rsc.li/rsc-advances

1. Introduction

In the field of nanomaterials, the fabrication of TiO_2–Ag heterostructures *via* green synthesis has emerged as a sustainable solution, replacing toxic chemical reducing agents with bio-derived secondary compounds.[1–4] The combination of silver (Ag) and TiO_2 is not simply a physical mixing but also creates heterojunctions that overcome the intrinsic drawbacks of pristine TiO_2, such as its wide bandgap (active only under UV light) and high photogenerated electron–hole recombination rate. Silver nanoparticles (AgNPs) act as electron accumulation centers, forming a Schottky barrier at the interface between TiO_2 and AgNPs, enabling AgNPs to act as electron "traps", promoting the efficient separation of photopassive electron–hole pairs. Furthermore, the presence of Ag also creates a surface plasmon resonance (SPR) effect, which extends light absorption to the visible region and enhances the generation of reactive oxygen species (ROS). Crucially, this system enables the sustained release of Ag^+ ions, providing superior antimicrobial activity under both light and dark conditions.[1–4]

Green synthesis strategies typically utilize plant extracts or microorganisms as stabilizing and reducing agents. Plant extracts (such as leaves, roots, or fruits), rich in polyphenols, flavonoids, and terpenoids, serve a dual function: their hydroxyl and carbonyl groups facilitate the bio-reduction of Ag^+ ions while simultaneously acting as capping agents to prevent nanoparticle aggregation.[5,6] Current research focuses on

[a]*Institute of Medicine and Pharmacy, Thanh Do University, Lai Xa, Hoai Duc, Hanoi, Vietnam*
[b]*Institute of Materials Science, Vietnam Academy of Science and Technology, 18 Hoang Quoc Viet, Nghia Do, Hanoi, Vietnam. E-mail: ntchinh@ims.vast.vn; thuychinhhn@gmail.com*
[c]*Graduate University of Science and Technology, Vietnam Academy of Science and Technology, 18 Hoang Quoc Viet, Nghia Do, Hanoi, Vietnam*
[d]*Hanoi National University of Education, 136 Xuan Thuy, Cau Giay, Hanoi, Vietnam*
[e]*Hanoi University of Industry, 298 Cau Dien, Tay Tuu, Hanoi, Vietnam*

achieving uniform dispersion of AgNPs on the surface or in the TiO_2 framework to optimize photocatalytic and antimicrobial performance. Generally, the TiO_2 substrate is synthesized first, then modified with a solution containing Ag^+ ions and plant extracts. The result is a TiO_2/Ag composite material with uniform nanoparticle size, high crystallinity, and superior activity due to the surface plasmon resonance (SPR) effect of AgNPs.[2,4] Controlling the extract concentration and the TiO_2/Ag ratio is crucial for optimizing application performance.

The utilization of *Eucalyptus* leaf extract (*Eucalyptus globulus* Labill) offers a highly promising approach. The abundant bioactive constituents in eucalyptus extract, particularly eucalyptol (1,8-cineol), polyphenols, flavonoids, and terpenes,[7–10] act as powerful reducing agents and stabilizers that govern particle size and morphology of resulting nanoparticles.[5,6,11] Previous studies have demonstrated that AgNPs were successfully synthesized using eucalyptus leaf extract with good antibacterial activity, effective photocatalytic degradation of dyes and low toxicity after photodegradation reaction.[12–15] In addition, eucalyptus leaf extract is also used in the synthesis of TiO_2 nanoparticles.[16] This demonstrated that using eucalyptus leaf extract as a reducing and stabilizing agent in the synthesis of TiO_2/Ag green nanocomposites holds considerable promise for optimizing photocatalytic and antimicrobial performance. Eucalyptus essential oil and extracts themselves already have natural antibacterial and antifungal properties,[7,11] therefore, when combined eucalyptus leaf extract with TiO_2 and Ag, the TiO_2/Ag@*Eucalyptus globulus* Labill (TiAg*x*PE) nanocomposite material creates a synergistic effect between the components in the particles in enhancing the antibacterial and photocatalytic effects of the particles.

While previous studies have extensively explored TiO_2/Ag composites for photocatalysis,[17–19] the majority of these existing methods rely on toxic chemical reducing agents, energy-intensive processes, or relatively high noble metal loadings to achieve satisfactory performance. Furthermore, these materials are predominantly evaluated for singular environmental applications. In contrast to these conventional approaches, the novelty of the present study lies in a synergistic, dual-functional design. Herein, we propose a facile and completely green synthesis of TiO_2/Ag nanocomposites (TiAg*x*PE) utilizing the dual action of *Eucalyptus globulus* Labill extract and PVA as eco-friendly reducing, capping, and structure-regulating agents. This method uniquely leverages the Zener pinning effect to stabilize the nanostructure, allowing for an exceptionally low Ag loading while maximizing the Schottky barrier-driven charge separation. Importantly, the presence of PVA not only enhances the synthesis yield[20] but also improves the anchoring of Ag nanoparticles onto the TiO_2 surface, thereby mitigating Ag leaching and ensuring safety for subsequent applications.

Distinct from previous works, this study comprehensively investigates the practical versatility of the synthesized nanomaterial through a dual-application strategy. Firstly, the nanocomposites were evaluated as highly efficient photocatalysts for environmental remediation. Remazol midnight black RGB (RGB) azo reactive dye was selected as the model pollutant. Although free of heavy metal ions, the discharge of RGB into wastewater severely impedes sunlight penetration, thereby inhibiting aquatic photosynthesis. Moreover, its inherent resistance to light, heat, and microbial degradation renders it highly recalcitrant in conventional biological treatment plants, leading to elevated oxygen demand and the formation of aquatic "dead zones".[21,22] The photocatalytic performance of the TiAg$_x$PE nanocomposites was systematically assessed under varying pH, catalyst dosage, irradiation time, and dye concentration.[23] Radical scavenging experiments employing isopropanol, EDTA, and L-ascorbic acid were subsequently conducted to identify the dominant reactive oxygen species governing the mineralization process.[24,25]

Secondly, expanding beyond wastewater treatment, the PVA-stabilized nanocomposites were integrated into a chitosan matrix to develop an active protective coating for the post-harvest preservation of grapes (*Vitis vinifera* L.). By embedding these nanomaterials into chitosan – a widely recognized biopolymer for food preservation[26–28] – a functional "multi-layered barrier" is formed. This system effectively regulates gas exchange and moisture transmission while preventing microbial infiltration, thus maintaining the structural integrity and sensory quality of the fruit. Ultimately, this dual-pronged approach highlights a sustainable pathway for advancing multipurpose active nanomaterials.

2. Materials and methods

2.1. Materials

Titanium isopropoxide (TTIP), silver nitrate, poly(vinyl alcohol) (PVA), glacial acetic acid (99.5%), L-ascorbic acid (LAA), ethylenediaminetetraacetic acid (EDTA), low molecular weight chitosan (CS), and Mueller Hinton agar (MH) were commercial-grade chemicals purchased from Thermo Fisher Scientific. Ethanol (99.5%) and isopropanol (IPA, 99.5%) were provided by GHTech (China). Remazol midnight black RGB (RGB) was purchased from DyStar Group (China). Tested bacterial strains including *E. coli*, *B. cereus, S. aureus* were sourced from ATCC (Manassas, USA) while *P. stutzeri* B27 (Gram-negative bacteria) was isolated from the coastal waters of Phu Quoc island, An Giang province, Vietnam. Fresh *Eucalyptus globulus* Labill leaves were collected from a local market in Hanoi city, Vietnam, thoroughly washed, and dried at 60 °C in an air convection oven until a constant weight was reached. The dried leaves were then ground into a fine powder and stored in an airtight zip-lock bags for further use.

2.2. Green synthesis of TiAg*x*PE nanocomposite

The TiAg*x*PE nanocomposite samples were synthesized *via* the sol–gel method using TTIP and $AgNO_3$ as precursors. Sample M0 (pristine TiO_2) was prepared by hydrolyzing 15 mL of TTIP in 150 mL of absolute ethanol for 60 minutes, followed by the addition of 15 mL of acetic acid. The mixture was magnetically stirred at 70 °C for 18 hours, then centrifuged and washed with an ethanol/water solution (70/30 v/v) to collect the solid precipitation. The solid was dried at 80 °C until reaching a constant mass and then calcined at 500 °C for 4 hours to

obtain TiO_2 nanoparticles. Sample M1 was synthesized following the same procedure as M0; however, during the hydrolysis step, a PVA solution (1.5 g PVA/30 mL distilled water) was added after the TTIP had hydrolyzed in ethanol. The mixture was magnetically stirred for an additional 30 minutes before adding acetic acid. Sample M2 followed the M1 procedure, with the exception that 15 mL of *Eucalyptus* extract (extraction ratio of 3 g *Eucalyptus globulus* Labill leaf powder/30 mL absolute ethanol, extraction temperature of 60 °C, extraction time of 2 hours) was added simultaneously with the acetic acid to facilitate the bio-reduction process. Samples M3, M4, and M5 were synthesized similarly to the M2 sample, with the simultaneous addition of Ag^+ ions from $AgNO_3$ solutions (containing 0.015 g, 0.05 g, and 0.15 g per 50 mL of distilled water, respectively) into the precursor solution before adding the PVA, *Eucalyptus* extract, and acetic acid. All samples were calcined at 500 °C for 4 hours to obtain the final materials. The studied samples and their compositions are summarized as follows: TiO_2, TiP (TiO_2/PVA), TiPE (TiO_2/PVA@*Eucalyptus globulus* Labill), TiAg0.1PE (TiO_2/Ag0.1/PVA@*Eucalyptus globulus* Labill), TiAg0.33PE (TiO_2/Ag0.33/PVA@*Eucalyptus globulus* Labill), TiAg1PE (TiO_2/Ag1/PVA@*Eucalyptus globulus* Labill).

2.3. Characterization of TiAg*x*PE nanocomposites

The TiAg*x*PE nanocomposite particles were characterized using various analytical techniques: Fourier-transform infrared spectroscopy (FTIR, Nicolet iS10, USA); dynamic light scattering (DLS) and electrophoretic light scattering (ELS) (Nanosize SZ-100Z2, Horiba, Japan); ultraviolet-visible diffuse reflectance spectroscopy (UV-vis DRS, UV 2600 spectrometer, Shimadzu, Japan); X-ray diffraction (XRD, CuK_α, Siemens D5000 X-ray diffractometer, Germany); field emission scanning electron microscopy (FESEM, S-4800, Hitachi, Japan); energy-dispersive X-ray mapping (EDX-Mapping, EDX detector, Oxford Instruments); high-resolution transmission electron microscopy (HR-TEM) and selected area electron diffraction (SAED) (JEM2100, JEOL, Japan); photoluminescence spectra (PL, an excitation wavelength of 355 nm, Varian spectrophotometer, Cary).

2.4. Electrochemical measurement

The working electrodes were prepared by mixing 9 mg of the powder sample (either TiPE or TiAg0.33PE) with 1 mg of polyvinylidene fluoride (PVDF, Thermo Fisher Scientific) binder. This mixture was dispersed in 1 mL of *N*,*N*-dimethylformamide (DMF, Thermo Fisher Scientific). To ensure a homogeneous suspension, the dispersion was subjected to continuous magnetic stirring followed by ultrasonication at a frequency of 40 kHz and a power of 100 W. Subsequently, the obtained uniform slurry was drop-cast onto a graphite plate (China) with a geometric working area of 1 cm^2. The coated graphite electrode was then dried in an oven at 80 °C until the solvent was completely evaporated. Electrochemical impedance spectroscopy (EIS) measurements were conducted in a 0.1 M Na_2SO_4 aqueous electrolyte using a standard three-electrode configuration. The sample-modified graphite plate served as the working electrode, alongside a platinum counter electrode and an Ag/AgCl reference electrode. The EIS tests were performed at the open-circuit potential (OCP) by applying a sinusoidal alternating current (AC) perturbation with a voltage amplitude of 10 mV over a frequency range from 100 kHz to 0.01 Hz.

The antibacterial activity of the TiAg*x*PE nanocomposite particles were determined using the agar well diffusion method.[29] Four bacterial strains were tested, including *E. coli* (EC), *S. aureus* (SA), *B. cereus* (BC), and *P. stutzeri* B27 (B27). The MH agar was employed as the culture medium. The powdered samples were dispersed in distilled water at a concentration of 0.1 g mL^{-1} *via* ultrasonication for 30 minutes at a frequency of 40 kHz. A volume of 50 μL of each suspension sample was added to each agar well. Ampicillin (0.125 mg mL^{-1}) served as the positive control, while distilled water was used as the negative control. After inoculation, the agar plates were initially incubated at 4 °C for 4 hours to allow for sample diffusion, followed by incubation at 37 °C. After 24 hours of cultivation, the plates were examined to measure the zone of inhibition (ZOI). The final diameter was determined by subtracting the diameter of the agar well from the total measured zone.

2.5. Photocatalytic ability study

The TiAg*x*PE nanocomposite particles were evaluated for their photocatalytic activity in the degradation of RGB dye under 200 W xenon light. The sample was centrifuged to extract the solution for UV-vis analysis (Libra S80 UV-Vis spectrometer, Biochrom, UK) at a maximum absorption wavelength of 600 nm. The dye photodegradation efficiency (H) was calculated using the following equation:

$$H\ (\%) = \left(1 - \frac{A_t}{A_0}\right) \times 100 \quad (1)$$

where, A_0 is the initial absorbance and A_t is the absorbance at time t of dye solution.

The factors influencing on the photocatalytic process including catalyst composition, pH, catalyst dosage, and initial dye concentration were investigated to evaluate catalytic efficiency.[30–32] Furthermore, the reusability of the catalyst was examined. To identify the primary reactive species, the effect of various scavengers on the photodegradation of RGB using TiAg*x*PE nanocomposites was evaluated. Specifically, the IPA, EDTA and LAA were employed as scavengers for hydroxyl radicals, holes (h^+), and superoxide radicals, respectively.[24,25] In these experiments, 5 mL of IPA or EDTA 0.1 M or 3.5 mL of LAA 0.01 M, was added to the dye solution prior to irradiation. The total organic carbon (TOC) of RGB dye, the solution after photocatalysis with TiPE and the solution after photocatalysis with TiAg0.33PE was determined according to TCVN 6634:2000 on a TOC-L device, Shimadzu, Japan.

2.6. Preservation of grapes

2.6.1. Preparation of the nanocomposite formulation for preservation. Four grams of CS were dissolved in 200 mL of a 2% acetic acid solution. Separately, 0.06 g of the nanocomposite particles were dispersed in 30 mL of distilled water using ultrasonication for 30 minutes, followed by magnetic

stirring for an additional 30 minutes. The resulting nanosuspension was then added dropwise into the CS solution and stirred for 4 hours on a magnetic stirrer at 400 rpm to ensure a homogeneous formulation. The samples were abbreviated as S1 (pure CS solution), S2 (CS + TiPE), S3 (CS + TiAg0.1PE), S4 (CS + TiAg0.33PE), S5 (CS + TiAg1PE).

To prepare films, 20 mL of each formulation was poured into each of three Petri dishes and allowed to dry naturally. The remaining solution was stored at room temperature for the fruit dipping process.

2.6.2. Grape preservation method. Green grapes (*Vitis vinifera* L.) were harvested from the same cluster, specifically selected for their firmness and absence of surface abrasions. The grapes were rinsed with distilled water and air-dried before the coating process.

The dipping process was performed in two stages: an initial immersion for 60 seconds, followed by air-drying, and a second immersion for 10 seconds. The treated grapes were then placed on racks and stored at a room temperature of approximately 30 °C for periodic monitoring.

The study samples consisted of the following groups: Grape0 (Control): untreated grapes; Grape1: grapes dipped in pure CS solution; Grape2: grapes dipped in CS + TiPE; Grape3: grapes dipped in CS + TiAg0.1PE; Grape4: grapes dipped in CS + TiAg0.33PE; Grape5: grapes dipped in CS + TiAg1PE.

2.6.3. Film characterization methods. The CS based nanocomposite films were characterized using mechanical properties (ASTM D882, Zwick testing machine, Germany), water vapor transmission rate – WVTR (ASTM E96), surface morphology (Olympus GX53 microscope, Japan). The antibacterial activity of these films was evaluated using the agar well diffusion method.

2.6.4. Evaluation of grape quality. The weight loss (WL) of the grapes was determined using the following equation:

$$\mathrm{WL}\ (\%) = \frac{m_0 - m_t}{m_0} \times 100 \quad (2)$$

where, m_0 is the initial mass of the grapes and m_t is the mass at time t.

The rotting rate (RR) of the grapes was calculated as follows

$$\mathrm{RR}\ (\%) = \frac{n_t}{n_0} \times 100 \quad (3)$$

where, n_0 is the initial number of the grapes and n_t is the number of spoiled grapes at time t.

The morphology of the grapes was documented using an Olympus SZ61 microscope and an Olympus GX53 microscope (Japan).

2.7. Data processing

The experiments were conducted in triplicate, and the results are presented as mean ± standard deviation. Data processing was performed with Microsoft Excel. Statistical significance between samples was determined using one-way analysis of variance (ANOVA) followed by the Tukey honestly significant difference (HSD) post-hoc test.

3. Results and discussion

3.1. Characterization of TiAg*x*PE nanocomposites

Fig. 1 presents FTIR spectra, UV-vis DRS, PL spectra, and XRD patterns of the synthesized TiAg*x*PE nanocomposites. As depicted in Fig. 1a, the FTIR spectra reveal the characteristic vibrational modes of the functional groups present in the materials. Notably, the broad absorption band centered at wavenumber of 3357 cm^{-1} and the relatively weaker peak at 1642 cm^{-1} are assigned to the O–H stretching and bending vibrations, respectively. These originate from surface-adsorbed water molecules and ambient moisture trapped within the structure of the materials. Furthermore, the complete absence of characteristic peaks in the 2800–3000 cm^{-1} range (typically corresponding to aliphatic C–H stretching) and around 1700 cm^{-1} (C=O stretching), confirms the successful thermal degradation and removal of PVA and residual organic compounds from the *Eucalyptus* extract during the calcination process. In the low-frequency region, a prominent and broad absorption band peaking at 658 cm^{-1} is exclusively attributed to the characteristic bending vibration of Ti–O–Ti linkages within the TiO_2 lattice.[4,33] The overall FTIR spectra of the TiAg*x*PE nanocomposites remain highly consistent with those of the pristine TiO_2 and TiPE samples. This structural congruence indicates that the incorporation of silver species into the TiO_2 matrix did not induce significant alterations or disruptions to the fundamental inorganic framework.

UV-vis DRS spectra in Fig. 1b reveal the optical absorption properties of the synthesized materials. All samples exhibit a sharp absorption edge in the UV region (below 400 nm), which exhibits the intrinsic band-to-band transition of electrons from the valence band to the conduction band in anatase TiO_2. Notably, the incorporation of silver species into the TiO_2 matrix (TiAg*x*PE nanocomposites) induces a distinct, broad absorption band in the visible light region. This enhanced visible-light absorption is primarily assigned to the localized surface plasmon resonance (LSPR) effect of the metallic AgNPs.[2,3] As the silver content increases (from TiAg0.1PE to TiAg1PE), the intensity of this visible absorption band progressively intensifies. This plasmonic enhancement significantly broadens the optical response of the nanocomposites, demonstrating their high potential for superior visible-light-driven photocatalytic performance compared to pristine TiO_2.

PL spectra (Fig. 1c) display broad emission bands centered in the range of 400–600 nm. The pristine TiPE sample exhibits a strong PL emission intensity, indicating a high recombination rate of photogenerated electron–hole pairs. Interestingly, the TiAg0.33PE sample exhibits a lower PL emission intensity than the TiPE sample. This demonstrates that the incorporated Ag nanoparticles effectively act as electron traps, capturing conduction band electrons and thereby suppressing the electron–hole pairs recombination process.

The crystalline structure and phase purity of the TiPE and TiAg0.33PE nanocomposites were confirmed by the XRD patterns (Fig. 1d). Both samples exhibit sharp and highly intense diffraction peaks, indicating excellent crystallinity. The

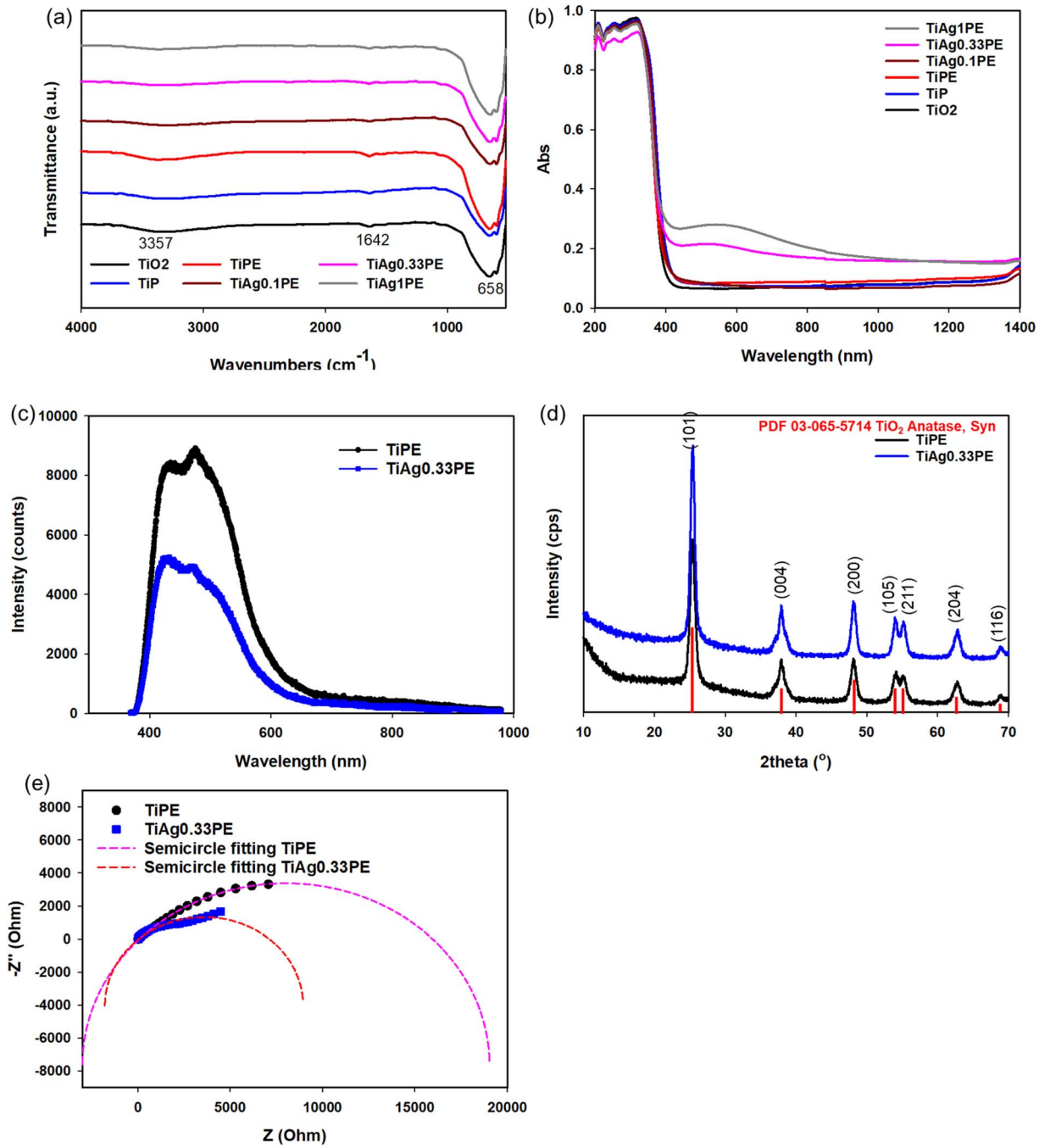

Fig. 1 FTIR spectra (a), UV-vis DRS (b), PL spectra (c), XRD patterns (d), and EIS spectra (Nyquist plot) (e) of TiAg*x*PE nanocomposites.

characteristic diffraction peaks at 2θ values of 25.4°, 37.8°, 48.0°, 53.9°, 55.1°, 62.7°, and 68.5° are perfectly indexed to the (101), (004), (200), (105), (211), (204), and (116) crystallographic planes of the anatase TiO_2 phase, respectively,[34] which is in excellent agreement with the standard data (PDF 03-065-5714). No diffraction peaks corresponding to the rutile or brookite phases are detected. This confirms that the synthesis conditions and subsequent heat treatment exclusively favored the formation of pure anatase TiO_2. The stabilization of this single-phase anatase structure can be attributed to the capping and structure-directing roles of the phytochemicals within the *Eucalyptus* extract during synthesis.

Although the addition of silver species slightly increased the intensity of the anatase peaks, characteristic diffraction peaks for metallic face-centered cubic (FCC) Ag are not explicitly observed. This absence is likely due to the low concentration of Ag, its high dispersion as ultra-small nanoparticles, and the strong overlapping of the primary Ag (111) peak ($2\theta \approx 38.1°$) with the intense (004) peak of anatase TiO_2. Moreover, the diffraction peaks of anatase TiO_2 in TiAg0.33PE are not shifted

to that of the TiPE, suggesting that Ag is mainly located on the surface or is minimally doped into the lattice of TiO_2. To quantitatively assess the impact of Ag incorporation on the crystallite size, the average crystallite size was calculated using the highest intensity (101) peak *via* the Scherrer equation:

$$D = \frac{K \times \lambda}{\beta \times \cos\theta} \quad (4)$$

where D is crystallite size (nm), K is the shape factor (0.89), λ is the X-ray wavelength (0.15406 nm), β is the full width at half-maximum (FWHM) in radians and θ is the Bragg diffraction angle.

Based on peak fitting using Origin software, the FWHM (β) values for TiPE and TiAg0.33PE are 0.63° (≈0.011 rad) and 0.54° (≈0.0094 rad), respectively. Consequently, the calculated average crystallite sizes are 12.77 nm for the TiPE and 14.88 nm for the TiAg0.33PE. This slight increase in crystallite size suggests that the incorporation of silver species into the nanocomposite system subtly alters the nucleation and growth

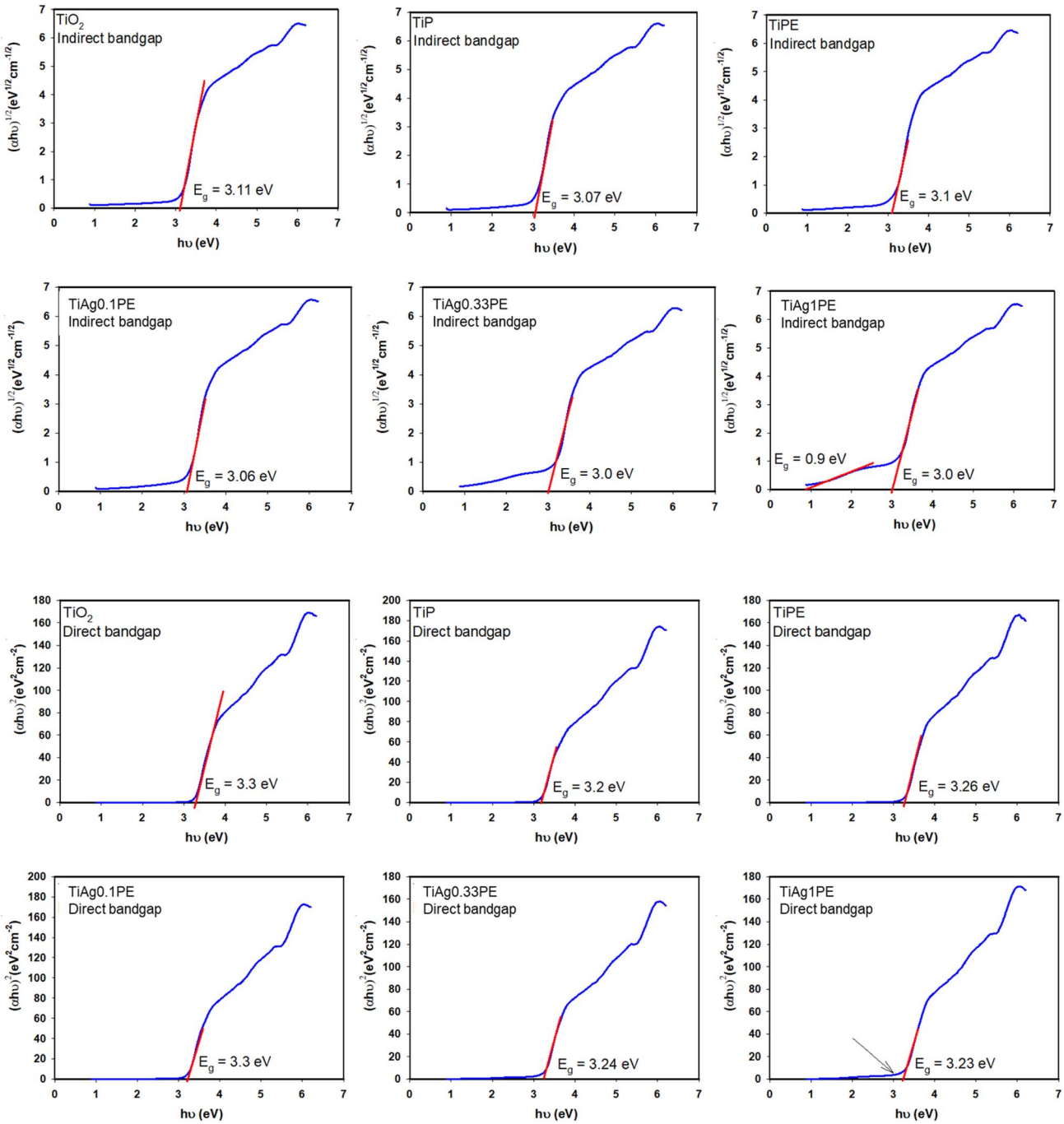

Fig. 2 Indirect bandgap and direct bandgap of TiAg*x*PE nanocomposites determined according to Tauc plot.

kinetics, promoting the crystalline development of the anatase lattice.

Fig. 1e presents the EIS spectra of TiPE and TiAg0.33PE. The EIS tests were performed at their respective open-circuit potentials (OCP), which were recorded as 0.229 V for the TiPE sample and 0.232 V for the TiAg0.33PE sample. The Nyquist plot for the TiAg0.33PE sample displays a substantially smaller semicircle radius compared to the TiPE sample, which corresponds to a lower charge transfer resistance at the interface. By fitting the experimental data with an equivalent circuit model, the charge transfer resistance (R_{ct}) values were determined, in which R_{ct} of TiPE is 15 875 Ω and R_{ct} of TiAg0.33PE is 7066 Ω. This reduction in R_{ct} directly confirms that Ag doping enhances the electrical conductivity and facilitates more efficient charge carrier transport at the electrode/electrolyte interface. This finding also confirms that the introduction of Ag not only mitigates charge carrier recombination but also improves electrical conductivity and interfacial charge transfer, factors which are highly favorable for enhancing the photocatalytic or electrochemical performance of the synthesized material.

Fig. 2 presents the Tauc plots and the corresponding estimated direct and indirect bandgap (E_g) values for the TiAg*x*PE nanocomposites. The incorporation of the organic modifiers (PVA and *Eucalyptus* extract) during the synthesis of TiO_2 (yielding TiP and TiPE), as well as the subsequent deposition of Ag species (TiAg*x*PE series), induces a modest reduction in both direct and indirect bandgap energies compared to pristine TiO_2. This marginal narrowing suggests that silver species are successfully incorporated into the TiO_2 system in two distinct forms: lattice dopants and surface-deposited nanoparticles. The doped Ag ions likely introduce localized mid-gap states between the valence and conduction bands, providing intermediate energy levels for electron excitation. Because these states are localized rather than forming a new continuous band, the shift in the bulk bandgap remains limited. Simultaneously, the presence of metallic Ag nanoparticles contributes to a significant absorption "tail" in the visible region, driven by the LSPR effect. These dual mechanisms including localized doping states and LSPR and induced sensitization express synergistically to enhance visible-light absorption and charge carrier separation (as evidenced by PL and EIS analyses), even though the intrinsic E_g values of the anatase phase are not drastically altered.

Fig. 3 displays the FESEM images of TiO_2 based nanocomposites. The surface morphology of the pristine TiO_2 sample exhibits a highly rough and heterogeneous structure, characterized by irregularly sized nanoparticles that undergo severe agglomeration into massive, dense clusters. The grain boundaries between individual particles are largely indistinguishable. This pronounced agglomeration is primarily driven by the high surface energy and thermodynamic instability inherent to bare TiO_2 nanoparticles, which thermodynamically favors spontaneous particle–particle interactions (*e.g.*, van der Waals forces) to minimize the exposed surface area.

Upon the introduction of PVA in the TiP sample, the microstructural evolution undergoes a distinct transformation. The TiP nanocomposite comprises well-defined, spherical particles with significantly enhanced size uniformity. The degree of nanoparticle agglomeration is remarkably reduced, revealing clear interparticle boundaries and a more ordered spatial arrangement. This structural improvement is fundamentally attributed to the steric stabilization provided by the PVA macromolecular chains. The PVA acts as an effective capping agent, wrapping around the TiO_2 nuclei to provide steric hindrance, thereby preventing their direct physical collision and fusion during the growth phase.

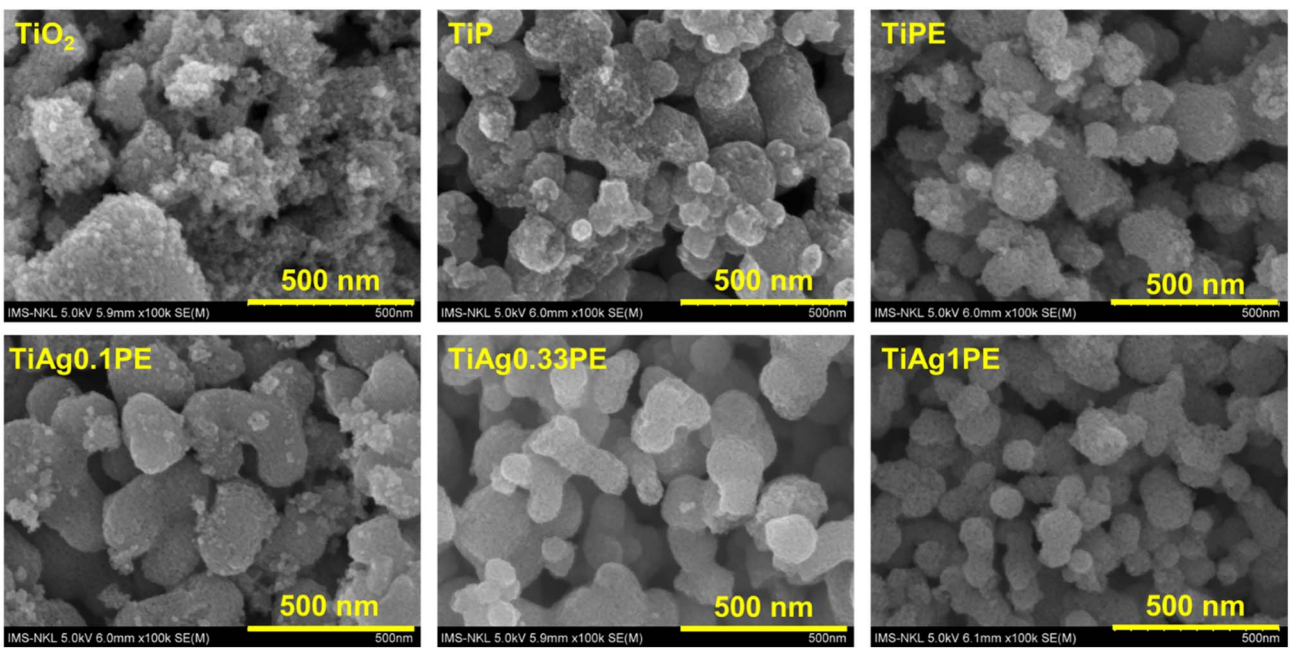

Fig. 3 FESEM images of TiAg*x*PE nanocomposites at the magnification of 100k times.

Interestingly, the TiPE nanocomposite displays a hybrid morphology, integrating the well-defined spherical domains characteristic of the TiP nanocomposite with localized heterogeneous aggregates resembling pristine TiO_2. The boundaries between certain particles become somewhat obscured compared to the TiP nanocomposite. This phenomenon can be elucidated by the complex phytochemical composition (*e.g.*, polyphenols and flavonoids) of the *Eucalyptus* extract. These biomolecules can form an intricate hydrogen-bonding network and cross-link with both the PVA matrix and the TiO_2 surface, promoting a secondary localized agglomeration and creating a continuous organic–inorganic interfacial matrix.

Furthermore, the incorporation and varying concentrations of silver significantly dictate the ultimate physicochemical regulation of the nanocomposites. At a low silver dosage (TiAg0.1PE), the material exhibits a highly porous matrix with massive particle clusters, representing a high degree of agglomeration and relatively poor structural uniformity. Conversely, the TiAg1PE sample (highest Ag content) demonstrates the most optimal morphological properties, featuring the lowest degree of agglomeration, reduced particle dimensions, and superior uniform dispersion. Mechanistically, an increased concentration of Ag nanoparticles deposited onto the TiO_2 surface strong electrostatic repulsion by altering the surface zeta potential. Moreover, these finely dispersed Ag domains act as physical barriers (the Zener pinning effect) that restrict grain boundary mobility. This pinning effect effectively prevents excessive grain growth and the fusion of TiO_2 nanoparticles during thermal treatment. Ultimately, the combination between steric hindrance, electrostatic forces, and Zener pinning regulates the microstructural evolution, ensuring a highly stable, uniform, and well-dispersed nanostructure.

Fig. 4 and 5 present the microstructural and elemental analyses, including the HR-TEM images of the TiPE and TiAg0.33PE samples, alongside the SAED pattern and EDX – elemental mapping of the TiAg0.33PE nanocomposite. Both TiPE and TiAg0.33PE exhibit a well-defined nanostructure composed of primary nanoparticles ranging from 10 to 20 nm in diameter. These nanoparticles exhibit a strong tendency to aggregate, forming highly porous clusters. Such a porous architecture is highly advantageous for photocatalytic applications, as it significantly enhances the specific surface area and facilitates the diffusion of reactant molecules to the active sites. At higher magnifications, the HR-TEM images reveal distinct and highly ordered lattice fringes, demonstrating the excellent crystallinity of the synthesized materials. For the TiAg0.33PE

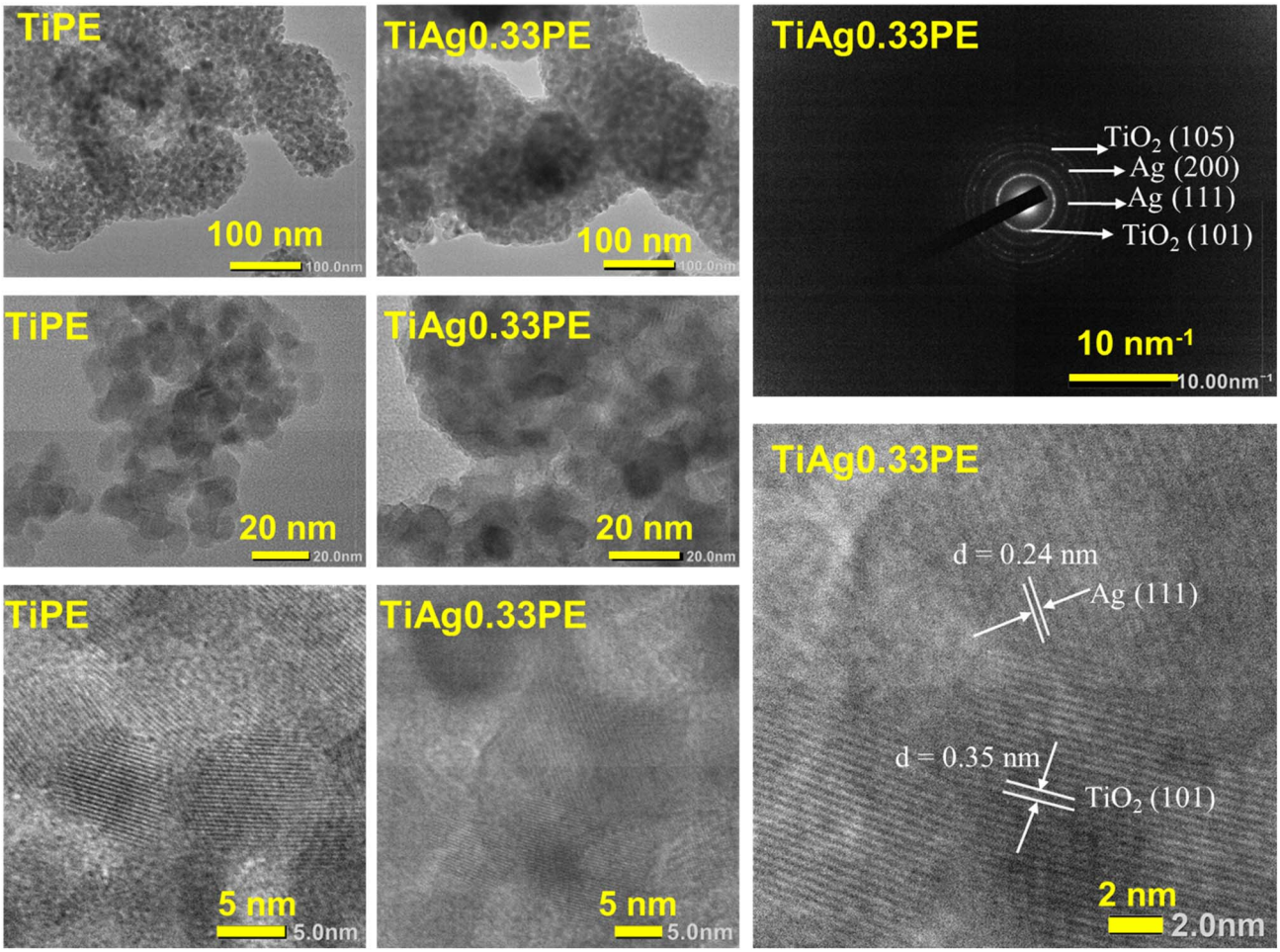

Fig. 4 HR-TEM images and SAED spectrum of TiPE and TiAg0.33PE nanocomposites.

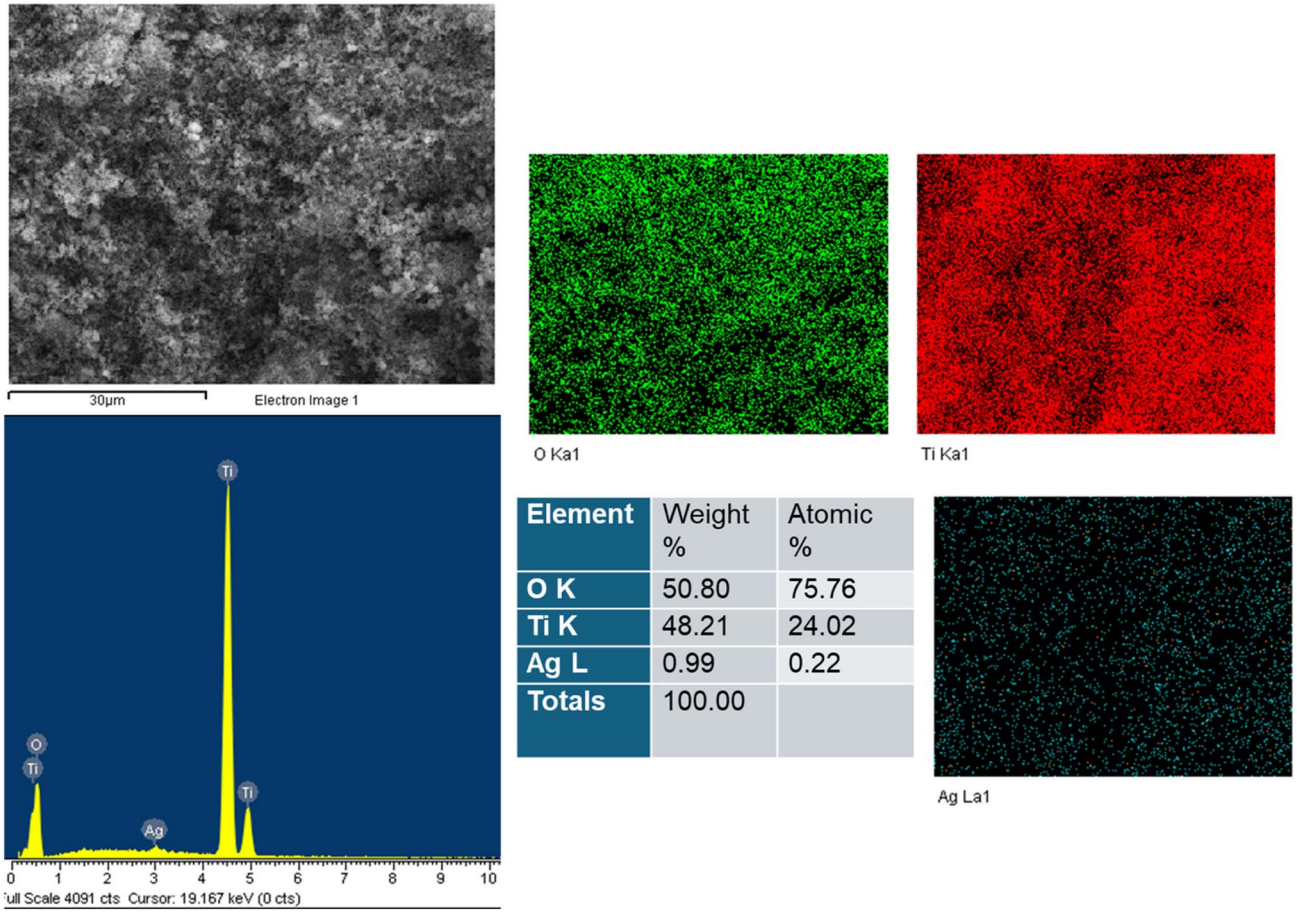

Element	Weight %	Atomic %
O K	50.80	75.76
Ti K	48.21	24.02
Ag L	0.99	0.22
Totals	100.00	

Fig. 5 EDX spectrum and element mapping of TiAg0.33PE nanocomposite.

nanocomposite, the highest magnification micrograph explicitly illustrates the coexistence of two distinct types of lattice fringes. The measured *d*-spacing of 0.35 nm is ascribed to the (101) crystallographic plane of anatase TiO_2, whereas the *d*-spacing of 0.24 nm corresponds to the (111) plane of face-centered cubic metallic silver. The intimate interfacial contact between these distinct lattice domains provides direct visual evidence that the Ag nanoparticles have been successfully anchored onto the TiO_2 surface. This tight interface is crucial for establishing a Schottky barrier, which serves to drive the efficient interfacial transfer of photogenerated electrons from TiO_2 to Ag, thereby mitigating charge recombination. The SAED pattern of the TiAg0.33PE sample displays well-defined concentric diffraction rings, confirming the polycrystalline nature of the nanocomposite. The indexed diffraction rings correspond perfectly to the (101) and (105) planes of the anatase TiO_2 phase, as well as the (111) and (200) planes of metallic Ag.[35–37] These crystallographic findings are in complete agreement with the HR-TEM observations, unambiguously verifying the formation of the TiO_2/Ag heterostructure. Furthermore, the EDX spectrum of the TiAg0.33PE sample confirms the presence of strong, characteristic peaks exclusively for Ti, O, and Ag, with no discernible impurity peaks, thereby indicating the high phase purity of the as-synthesized nanocomposite.[37] Quantitative analysis reveals a mass composition of 50.80% O, 48.21% Ti, and 0.99% Ag. The detected silver content of approximately 1 wt% corroborates that the noble metal was successfully incorporated into the host matrix at the targeted trace concentration. The EDX elemental mapping further elucidates the spatial distribution of these elements. While Ti and O are densely and continuously distributed, forming the structural backbone of the TiO_2 matrix, the Ag signals, despite their lower density, are uniformly dispersed across the entire scanned area without any localized agglomeration. This optimal and homogeneous dispersion of Ag nanoparticles on the semiconductor support is of paramount importance. It not only maximizes the density of catalytically active sites but also effectively induces localized surface plasmon resonance and acts as an electron sink. Consequently, this synergistic effect drastically suppresses the recombination of electron–hole pairs, leading to a profound enhancement in the overall photocatalytic performance.

Table 1 summarizes the zeta potential values of the synthesized TiO_2-based nanocomposites, providing crucial insights into their colloidal stability in aqueous suspension. The absolute values of the zeta potential serve as a reliable indicator of electrostatic stabilization. Notably, the TiAg1PE sample exhibits the most negative surface charge with a zeta potential of −42.53

Table 1 Zeta potential of TiO_2 based nanocomposite samples

Sample	TiO_2	TiP	TiPE	TiAg0.1PE	TiAg0.33PE	TiAg1PE
Zeta potential (mV)	-12.30 ± 0.42	-15.40 ± 2.67	-31.55 ± 2.82	-35.50 ± 0.28	-39.95 ± 1.38	-42.53 ± 0.92

$\pm$ 0.92 mV. This highly negative value signifies robust electrostatic repulsion between adjacent nanoparticles, effectively preventing particle agglomeration and ensuring excellent colloidal stability. Similarly, the TiPE, TiAg0.1PE, and TiAg0.33PE samples demonstrate high dispersion stability, with zeta potentials of -31.55 ± 2.82 mV, -35.50 ± 0.28 mV, and -39.95 ± 1.38 mV, respectively. Because their absolute values exceed the conventional stability threshold of 30 mV, these colloidal systems are considered highly stable.

In contrast, the pristine TiO_2 (-12.30 ± 0.42 mV) and TiP (-15.40 ± 2.67 mV) samples exhibit zeta potentials significantly closer to zero. These lower absolute values indicate insufficient repulsive forces, confirming their poor dispersion stability and higher tendency to coagulate. The remarkable enhancement in the stability of the TiPE sample highlights the synergistic capping effect of PVA and the plant extract. The molecular structure of PVA provides steric hindrance, while the abundant functional groups from the *Eucalyptus* extract likely impart a strong negative surface charge. This dual stabilization mechanism efficiently controls the nucleation and restricts particle agglomeration during the growth process. Furthermore, the incorporation of silver species into the TiO_2 matrix correlates with a progressive increase in the absolute negative zeta potential. This continuous enhancement in stability implies that the anchoring of Ag nanoparticles favourably alters the surface chemistry of the composites, potentially by modifying the surface charge distribution.

The antibacterial efficacy of the synthesized TiO_2-based nanocomposites was evaluated against four bacterial strains (*E. coli*, *S. aureus*, *B. cereus*, and *P. stutzeri* B27), revealing a significant dose-dependent response to silver incorporation. As indicated in Table 2 and Fig. 6, the pristine TiO_2, TiP, and TiPE samples exhibited no antibacterial activity, yielding a ZOI of 0 mm across all tested strains. However, the introduction of silver drastically transformed the materials into potent antimicrobial agents, with the TiAg1PE nanocomposite demonstrating the highest efficacy, producing ZOI values ranging from 5 mm against *B. cereus* to 12 mm against *S. aureus* and *P. stutzeri* B27. The TiAg*x*PE nanocomposites in this study exhibit notable antibacterial activity, similar to others reported.[3,4,34] Notably, all of these Ag-doped nanocomposites significantly outperformed the commercial antibiotic ampicillin, which only showed a minimal 4 mm ZOI against *S. aureus* and no activity against the other strains. In this hierarchical system, each component plays a specific role: the plant extract functions as a crucial green reducing and capping agent that ensures the uniform dispersion of Ag nanoparticles while its inherent phytochemicals may synergistically enhance the composite's overall biological interactions, whereas the porous TiO_2 matrix acts as a robust structural support to prevent silver agglomeration, thereby maximizing the active surface area. The profound bactericidal performance of the TiAg*x*PE nanocomposites is governed by several interacting mechanisms driven primarily by the silver species. Upon contact with the aqueous biological environment, the anchored Ag nanoparticles continuously release Ag^+ ions, which are electrostatically attracted to the negatively charged bacterial cell membranes, ultimately disrupting membrane permeability and causing the leakage of vital intracellular components.[4,5] Furthermore, the small-sized nanocomposites can physically adhere to and penetrate the cell envelope, inducing irreversible structural damage. Once internalized, the highly reactive Ag^+ ions exhibit a strong affinity for thiol (–SH) groups in essential cellular enzymes and proteins, effectively deactivating critical metabolic pathways and hindering DNA replication. Concurrently, the interfacial contact between the nanocomposite and the bacteria induces localized oxidative stress, generating highly reactive oxygen species (ROS) that further degrade cellular lipids, proteins, and nucleic acids, cumulatively resulting in total bacterial cell death.

Table 2 Antibacterial activity of TiO_2 based nanocomposite samples

		ZOI (mm)			
No.	Sample	EC	SA	BC	B27
1	TiO_2	0	0	0	0
2	TiP	0	0	0	0
3	TiPE	0	0	0	0
4	TiAg0.1PE	6	9	3	10
5	TiAg0.33PE	7	11	4	11
6	TiAg1PE	8	12	5	12
7	Ampicillin	0	4	0	0
8	Negative control	0	0	0	0

3.2. Photocatalytic capacity of TiAg*x*PE nanocomposite in reactive dye degradation

The photocatalytic performance of the synthesized TiO_2-based nanocomposites was systematically evaluated through the degradation of RGB dye under varying operational conditions. The results obtained are presented in Fig. 7. The blank experiment showed negligible dye removal, whereas all composite samples achieved high degradation efficiencies of approximately 90–100% within 30 minutes of irradiation. Among the tested materials, TiPE and TiAg0.33PE demonstrated the highest photocatalytic efficiency (Fig. 7a). The effectiveness of this process is highly dependent on several physicochemical parameters; for instance, increasing the catalyst dosage from 0.2 to 0.6 mg mL^{-1} significantly enhanced efficiency by providing a greater number of active sites and a larger surface

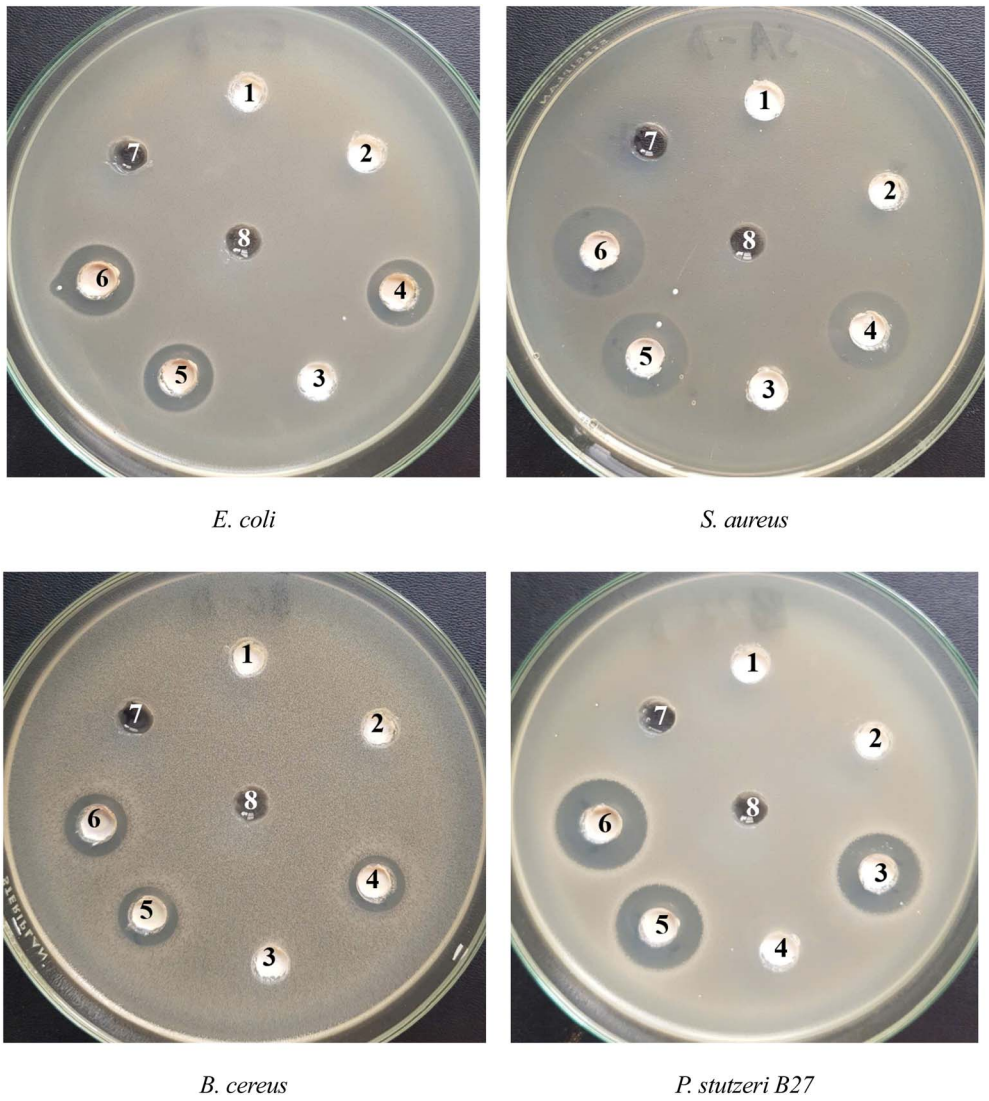

Fig. 6 Antibacterial activity of TiAg*x*PE nanocomposites. Numbers indicate the sample IDs as defined in Table 2.

area for dye adsorption and photon absorption (Fig. 7b). Furthermore, the suitable environment for the system was determined to be pH 4 solution, which facilitates strong electrostatic attraction between the positively charged catalyst surface and the anionic dye molecules, whereas efficiency gradually declined at higher pH levels (Fig. 7c). Conversely, increasing the initial RGB concentration from 15 ppm to 60 ppm led to a notable decrease in degradation efficiency, primarily due to the light-shielding effect and the rapid saturation of active sites by the massive adsorption of dye molecules (Fig. 7d). The significance of this adsorption was further highlighted in the contact time survey, which revealed that a substantial portion of the dye was removed during the 30-minute dark phase, indicating that the exceptional removal efficiency stems from a synergistic combination of robust dark adsorption – supported by the highly porous structure and functional groups of the *Eucalyptus* extract and PVA-followed by rapid photooxidation under light (Fig. 7e). In terms of stability, although the catalysts maintained 100% efficiency in the first cycle, their reusability experienced a gradual decline to approximately 90% for the TiPE sample and 73.33% for the TiAg0.33PE solution after five consecutive cycles (Fig. 7f). This gradual decline is fundamentally governed by the unavoidable loss of catalyst mass during the recovery process. As detailed in the experimental records, the initial mass of 200 mg for the TiPE sample was reduced to 160 mg after five cycles, representing a 20% mass loss due to repeated centrifugation and washing steps. A similar trend was observed for the TiAg0.33PE sample, which experienced a mass reduction to 101 mg (49.5% loss). The close correlation between the percentage of mass loss and the decrease in catalytic activity confirms that the intrinsic active sites of the TiPE and TiAg0.33PE samples remain largely functional. However, the TiAg0.33PE sample experienced greater mass loss, resulting in a greater reduction in catalytic activity. Furthermore, the potential deposition of organic intermediate species on the catalyst surface may contribute to

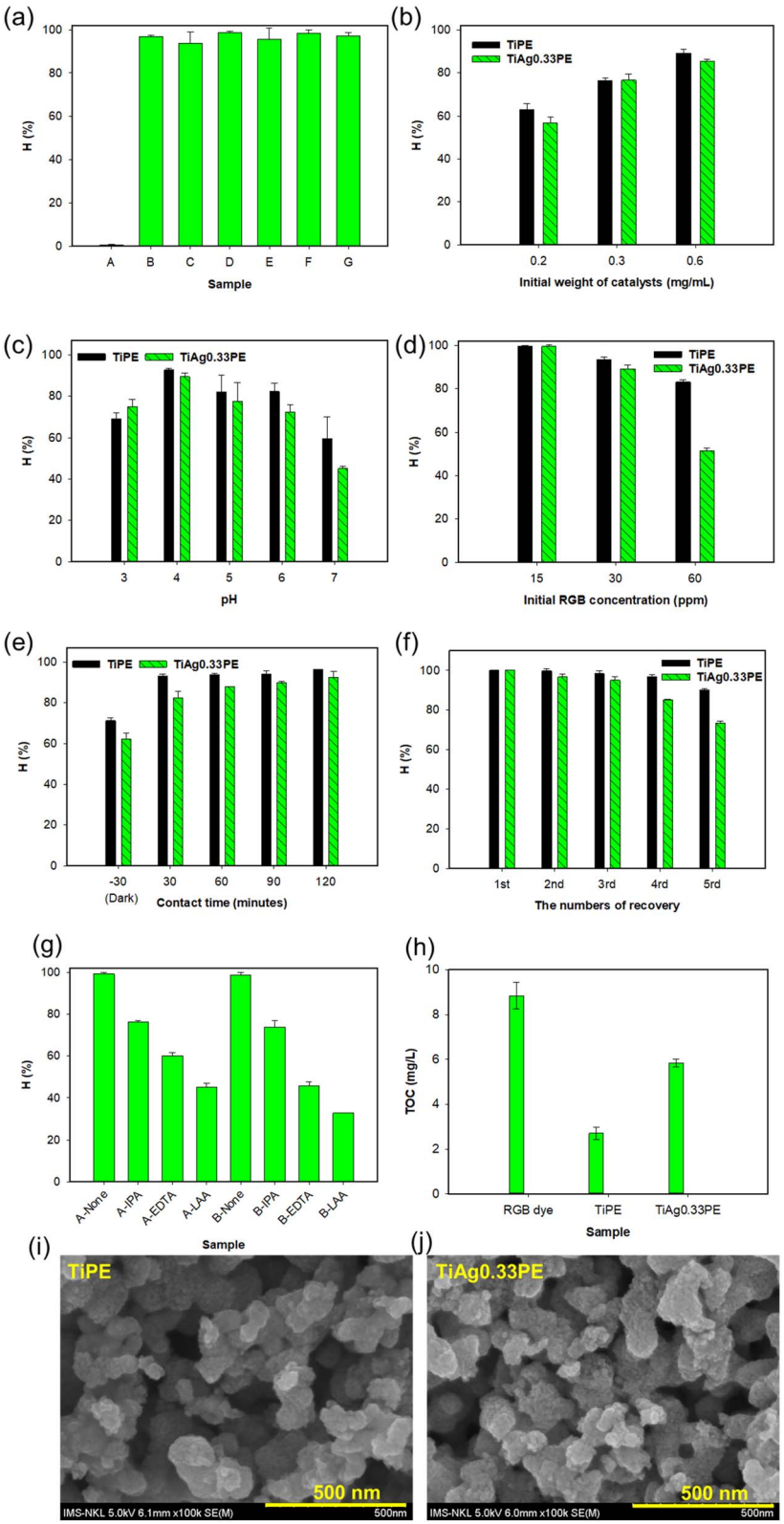

Fig. 7 Photocatalysis activity of $TiAg_xPE$ nanocomposites. (a) Effect of different samples (A: RGB dye, B: TiO_2, C: TiP, D: TiPE, E: TiAg0.1PE, F: TiAg0.33PE, G: TiAg1PE; initial concentration of RGB dye of 30 ppm, pH 5, contact time of 30 minutes, initial weight of catalysts of 1 mg mL^{-1}, volume of dye of 50 mL); (b) effect of initial weight of catalysts (initial concentration of RGB dye of 30 ppm, pH 5, contact time of 60 minutes, volume of dye of 50 mL); (c) effect of pH (initial concentration of RGB dye of 30 ppm, contact time of 60 minutes, initial weight of catalysts of 0.3 mg mL^{-1}, volume of dye of 50 mL); (d) effect of initial RGB concentration (contact time of 60 minutes, initial weight of catalysts of 0.3 mg mL^{-1}, pH 4, volume of dye of 50 mL); (e) effect of contact time (initial concentration of RGB dye of 30 ppm, initial weight of catalysts of 0.3 mg mL^{-1}, pH 4, volume of dye of 50 mL); (f) effect of the numbers of recovery (initial concentration of RGB dye of 30 ppm, initial weight of catalysts

a slight reduction in available active sites. Overall, the TiPE and TiAg0.33PE nanocomposites demonstrate commendable stability and durability, which are essential for practical wastewater treatment. To address the challenge of catalyst recovery and minimize mass loss in practical applications, future strategies could focus on the immobilization of these nanocomposites onto macroscopic scaffolds, such as porous membranes, ceramic foams, or 3D-printed polymer substrates. By transitioning from a suspended powder system to an immobilized assembly, the separation process can be simplified, effectively eliminating the need for energy-intensive centrifugation and ensuring long-term operational stability without significant efficiency trade-offs.

To elucidate the underlying degradation mechanism, free radical trapping experiments using the IPA, EDTA, and LAA were performed. The results confirmed that superoxide radicals ($^{\bullet}O_2^-$) and photogenerated holes (h^+) are the primary reactive species driving the oxidative cleavage of the dye. In contrast, the addition of IPA results in minimal inhibition, indicating that hydroxyl radicals ($^{\bullet}OH$) serve only a secondary function in the degradation process (Fig. 7g). This mechanism is further supported by the TOC analysis in Fig. 7h, which shows a significant decrease in organic carbon content, confirming the effective mineralization of the 30 ppm RGB dye by the TiPE and TiAg0.33PE nanocomposites. The superior performance of the TiAg0.33PE nanocomposite is attributed to the synergistic integration of the TiO_2 matrix and Ag nanoparticles. The incorporation of metallic silver establishes a Schottky barrier at the TiO_2–Ag interface, which acts as an efficient electron sink. This facilitates unidirectional charge transfer and effectively suppresses the undesirable recombination of electron–hole pairs. Consequently, the extended lifespan of the charge carriers promotes the continuous and robust generation of highly reactive oxygen species, which ultimately mineralize the complex structure of the RGB molecules into simpler, less toxic products. Compared with the recent reports by Rudzani Ratshiedana[35] and Noor J. Ridha,[37] the TiAg0.33PE nanocomposite in this study – despite having a much lower Ag content – demonstrates comparable photocatalytic degradation efficiency alongside superior antibacterial activity.

The structural and morphological stability of the photocatalysts after multiple uses was further verified by FESEM analysis and shown in Fig. 7i and j. As can be seen that the morphology of both TiPE and TiAg0.33PE samples was remarkably maintained after five consecutive photocatalytic cycles. The FESEM images reveal that the primary spherical geometry and size distribution of the TiO_2 nanoparticles remain essentially unchanged compared to their initial state. Although a slight change in the macroscopic color of the recovered powders was observed – likely due to the strong adsorption of residual dye molecules or refractory intermediate byproducts onto the active surface sites – the underlying inorganic framework remains structurally robust. This preservation of the nanostructure, despite the surface adsorption phenomena, confirms the high mechanical and chemical durability of the TiPE and TiAg0.33PE nanocomposites, making them highly suitable for sustainable environmental remediation.

3.3. Characterization of chitosan containing TiAg*x*PE nanocomposite and application in grape storage

The TiO_2 based nanocomposites have been added to the chitosan (CS) matrix for grape preservation. The structure and properties of CS based films have been evaluated and presented in Fig. 8. As illustrated in the FTIR spectra (Fig. 8A), the pristine CS film (S1) and the nanocomposite films (S2–S5) exhibit highly consistent spectral profiles, featuring a prominent broad band at 3363 cm^{-1} corresponding to the overlapping stretching vibrations of O–H and N–H groups, alongside characteristic peaks for C–H stretching (2917 cm^{-1}), amide I (1646 cm^{-1}), amide II (1577 cm^{-1}), and glycosidic linkages (1069 cm^{-1}).[34] The absence of significant band shifts or new functional group peaks confirms that the fundamental chemical backbone of the CS matrix remains structurally intact, suggesting that the incorporation of the inorganic TiAgPE nanoparticles is primarily governed by physical interactions, such as hydrogen bonding, rather than covalent modifications. However, the physical inclusion of these rigid nanoparticles disrupts the continuous intermolecular hydrogen-bonding network of the neat polymer, which directly impacts the mechanical integrity of the composite films. Consequently, compared to the pristine S1 film-which exhibits a robust tensile strength of approximately 25 MPa and an elongation at break of 62%-the addition of the nanoparticles induces a notable reduction in both parameters across the S2 to S5 formulations, as the fillers restrict polymer chain mobility under tensile stress and act as stress concentration points that initiate premature microcracking (Fig. 8B). Although the incorporation of these nanoparticles results in a compromise in mechanical flexibility, this specific microstructural modification imparts crucial barrier properties that are highly advantageous for food packaging.[28,38] First, the dispersed TiAg*x*PE nanoparticles occupy the free volume within the biopolymer matrix, creating a complex "tortuous path" that effectively physically hinders the permeation of water vapor and environmental gases. Second, the inorganic nature of the TiO_2/Ag fillers acts as a potent UV-blocking shield, which is essential to prevent the photooxidation and nutrient degradation of the packaged fruit. Finally, the embedding of these active fillers transforms the passive chitosan film into a biologically active barrier capable of continuous antimicrobial action. Therefore, in the context of postharvest preservation, the partial loss in mechanical

of 4 mg mL^{-1}, contact time of 120 minutes, pH 4, volume of dye of 50 mL); (g) effect of scavengers (A: TiPE; B: TiAg0.33PE; initial concentration of RGB dye of 30 ppm, initial weight of catalysts of 0.6 mg mL^{-1}, contact time of 120 minutes, pH 4, volume of dye of 50 mL, 5 mL IPA 99.5%, 5 mL of EDTA 0.1 M, 3.5 mL of LAA 0.01 M); (g) TOC values of 30 ppm RGB dye solution (RGB dye), the solution sample after photocatalysis with TiPE (TiPE) and the solution sample after photocatalysis with TiAg0.33PE (TiAg0.33PE) (according to TCVN 6634:2000); (i) FESEM images of TiPE sample after dye photocatalysis; (j) FESEM images of TiAg0.33PE sample after dye photocatalysis.

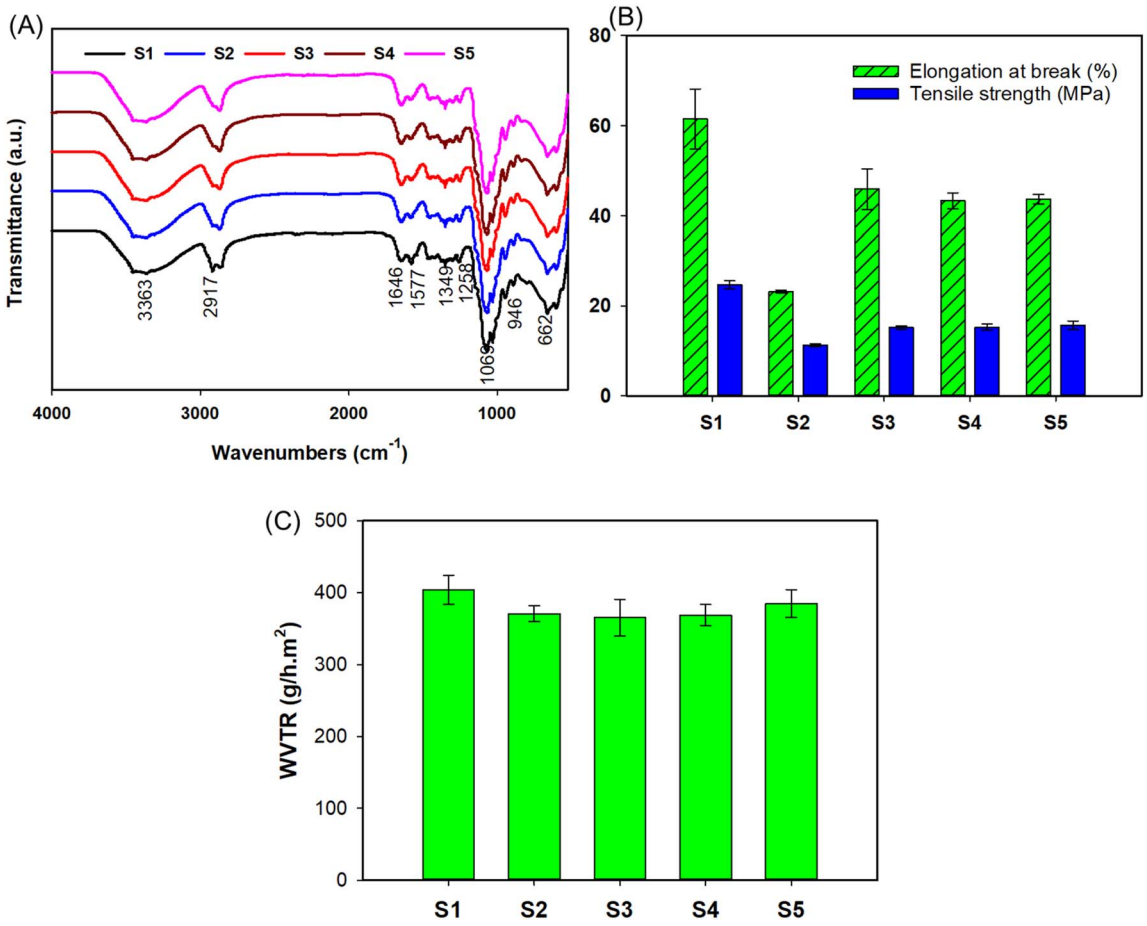

Fig. 8 IR spectra (A), mechanical properties (B) and WVTR (C) of CS based nanocomposite films containing TiAg*x*PE nanoparticles.

ductility is an acceptable and necessary trade-off to achieve a multifunctional protective envelope. The WVTR value of the intermediate nanocomposite films (S2–S4) notably decreases from 404.58 g h^{-1} m^{-2} in the control film to 371.04–385.13 g h^{-1} m^{-2} (Fig. 8C). This reduction is driven by the "tortuous path" mechanism, wherein the dispersed, impermeable inorganic nanoparticles force diffusing water vapor molecules to navigate a much longer, complex route through the polymer matrix.[38,39] Interestingly, the S5 sample displays a slight rebound in WVTR value compared to the S2–S4 formulations. This phenomenon suggests that at the higher Ag loading of TiAg1PE, the system reaches a critical loading threshold. At this stage, localized nanoparticle agglomeration may occur, generating microscopic voids at the organic-inorganic interface that slightly facilitate moisture transmission. It is important to note that while S4 (CS + TiAg0.33PE) represents the optimal configuration for a physical barrier, the higher Ag content in S5 provides a superior antimicrobial shield and better metabolic regulation during fruit storage.

Surface morphology of CS based nanocomposite films containing TiAg*x*PE nanoparticles has been assessed using inverted microscopy and presented in Fig. 9. In the CS + TiPE and lower-silver formulations (CS + TiAg0.1PE), the nanoparticles are reasonably distributed across the polymer matrix with smaller, scattered aggregates. However, as the silver concentration increases, the density of the nanoparticles noticeably intensifies, leading to more pronounced localized agglomeration. This phenomenon is explicitly visible as larger, dense bright clusters heavily distributed on the surfaces of the CS + TiAg0.33PE and CS + TiAg1PE films. This microstructural evolution directly dictates the mechanical and barrier properties of the packaging films. The physical inclusion of these rigid inorganic nanoparticles inherently disrupts the continuous intermolecular hydrogen-bonding network of the neat chitosan matrix. Consequently, the localized agglomerates act as structural defects and stress concentration points under physical load, which explains the noticeable reduction in both tensile strength and elongation at break compared to the pristine film.

The antibacterial performance of the nanocomposite films is fundamentally dictated by the silver content and the structural composition of the matrix. Agar diffusion assays demonstrate that the pristine CS (S1) and CS + TiPE (S2) films lack observable inhibitory effects, yielding a ZOI of 0 mm (Table 3). Conversely, the incorporation of Ag imparts significant bactericidal capabilities (3–4 mm). Notably, the S5 film (CS + TiAg1PE) achieved the highest efficacy, exhibiting a 4 mm ZOI against *E. coli*. The robust antibacterial activity of the Ag-doped films stems primarily from the continuous release of Ag^{+} ions, which

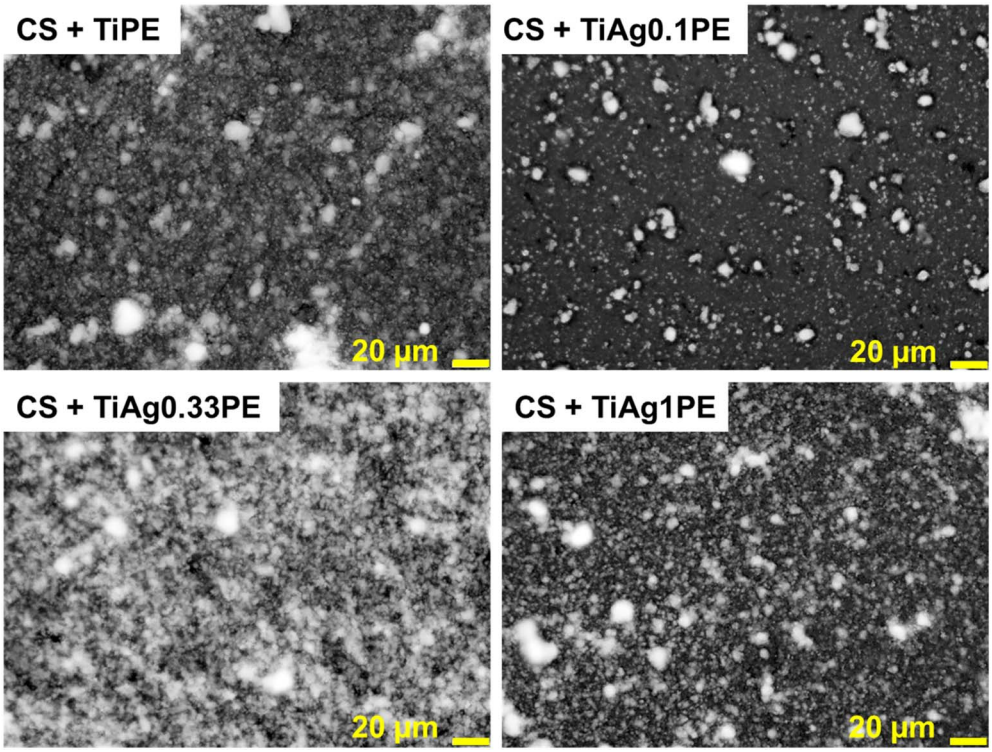

Fig. 9 Morphology of CS based nanocomposite films containing $TiAg_xPE$ nanoparticles.

Table 3 Antibacterial ability against *E. coli* of CS based nanocomposite films containing $TiAg_xPE$ nanoparticles

Sample	ZOI (mm)	Agar dish image
CS (S1)	0	
CS + TiPE (S2)	0	
CS + TiAg0.1PE (S3)	3	
CS + TiAg0.33PE (S4)	3	
CS + TiAg1PE (S5)	4	
Ampicillin (Amp)	0	
Cephalexin (Ceph)	40	

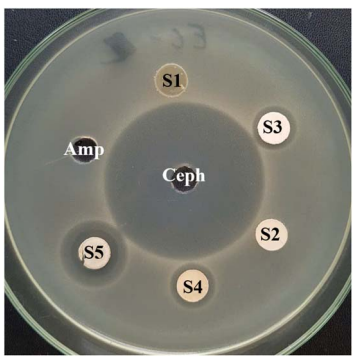

interact electrostatically with negatively charged bacterial cell membranes.[34] The synergistic action of these metal ions and the active functional groups of the matrix ultimately leads to severe membrane disruption, the leakage of vital intracellular components, and irreversible cellular death.

Fig. 10 and 11 present the stereo microscopy and inverted microscopy of grapes covered with the CS based nanocomposite films containing $TiAg_xPE$ nanoparticles. The stereo microscopy images in Fig. 10 offer a macroscopic view of the physical appearance of the grape surfaces. The uncoated control sample (Grape0) exhibits a natural, bare green surface. Upon treatment with the pure CS solution (Grape1), the surface retains its natural color but appears to have a subtle, homogeneous, and transparent film layer. With the introduction of the nanoparticles (Grape2 to Grape5), distinct tiny white speckles become visible across the green epidermis. The density of these white spots progressively intensifies from Grape2 (CS + TiPE) to Grape5 (CS + TiAg1PE). In the Grape5 sample, these particles

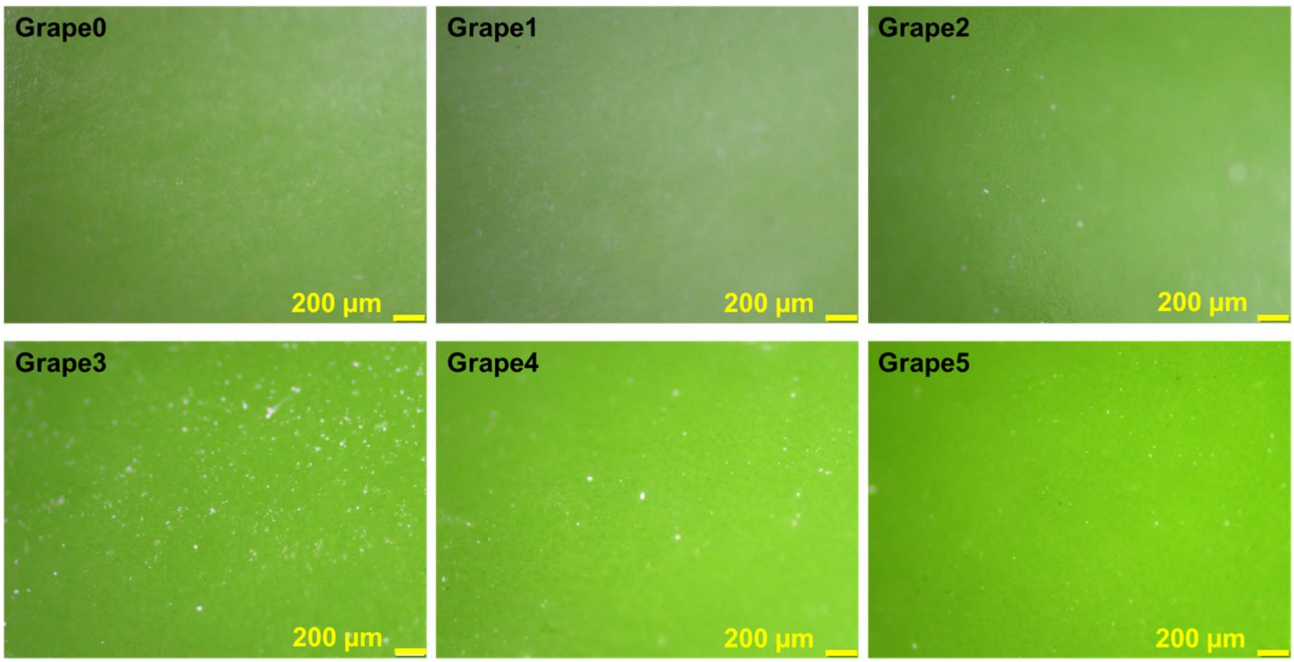

Fig. 10 Stereo microscopy images of grapes stored by CS based nanocomposite films containing TiAg*x*PE nanoparticles.

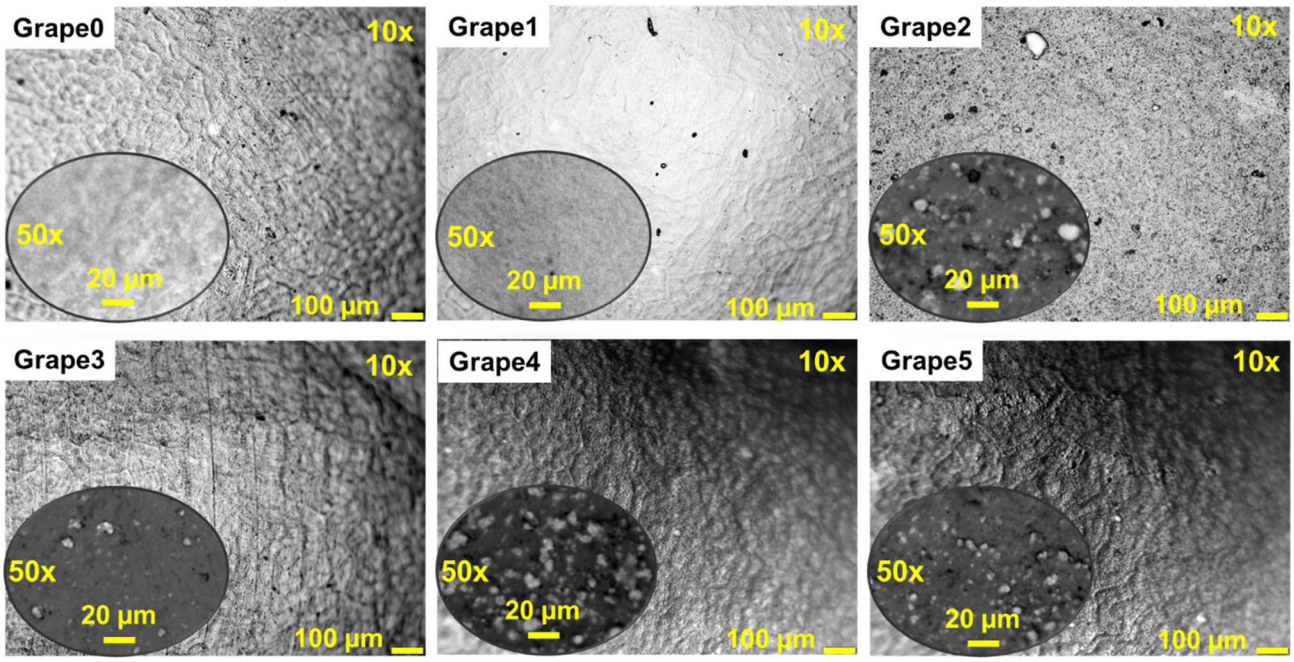

Fig. 11 Inverted microscopy images of grapes stored by CS based nanocomposite films containing TiAg*x*PE nanoparticles. 10×: images at the magnification of 10×, 50× insets: images at the magnification of 50×.

are densely and relatively uniformly distributed across the entire visible surface, visually confirming that the nanoparticles are successfully dispersed within the CS coating directly on the fruit's skin. The inverted microscopy images in Fig. 11, particularly with the 50× magnification inserts, provide a deeper insight into the micro-topography of the coated grape skins. At the magnification of 10×, the pristine epidermis of Grape0 displays a naturally rough texture with distinct cellular outlines and inherent micro-crevices. In contrast, the Grape1 sample shows a much smoother topography, indicating that the neat CS matrix effectively fills the epidermal grooves to form a continuous protective barrier. For the nanocomposite-coated samples (Grape2 to Grape5), the surface of the grape skin becomes rougher and more uneven. At the magnification of 50× (50×

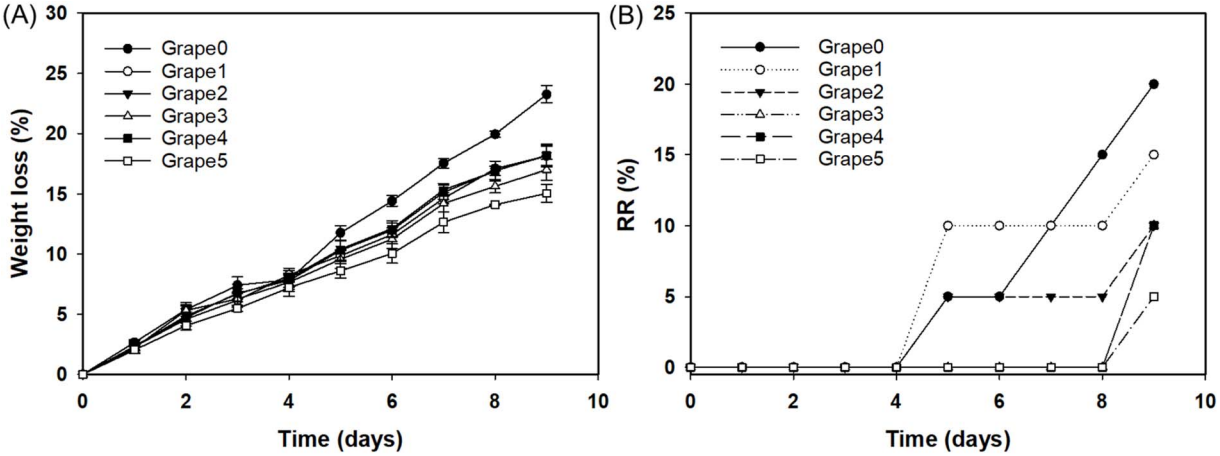

Fig. 12 Weight loss and RR of grapes stored by CS based nanocomposite films containing TiAg*x*PE nanoparticles.

insets), these images explicitly reveal the inorganic nanoparticles embedded within the polymeric matrix on the fruit surface. Consistent with previous morphological observations of the films, the incorporated nanoparticles exhibit a tendency to form localized clusters. As the silver concentration increases (from Grape3 to Grape5), these clusters become larger, denser, and more prominent. The Grape4 and Grape5 samples display highly concentrated bright agglomerates strongly adhered to the grape skin.

The weight loss and RR of grapes stored by CS based nanocomposite films containing TiAg*x*PE nanoparticles are shown in Fig. 12. The physiological efficacy of the synthesized nanocomposite coatings for postharvest preservation was quantitatively evaluated by monitoring the weight loss and rotting rate (RR) of fresh grapes over a 9-day storage period. As expected, moisture transpiration and cellular respiration led to a continuous increase in weight loss across all samples. However, the uncoated control (Grape0) exhibited the most rapid physiological degradation, culminating in a severe weight loss of approximately 23% by day 9, whereas the application of a neat chitosan coating (Grape1) mitigated this loss to roughly 18%. The incorporation of TiAg*x*PE nanoparticles further enhanced the moisture barrier capabilities of the films, progressively minimizing weight loss as the nanoparticle concentration increased, with the Grape5 sample (coated with CS + TiAg1PE) demonstrating optimal moisture retention by restricting the total weight loss to merely 15%. This improvement indicates that the dispersed inorganic nanoparticles effectively create a tortuous pathway within the polymer matrix, restricting the diffusion of water vapor. Concurrently, the rotting rate served as a macroscopic indicator of the coatings' antimicrobial performance. The control and neat CS-coated grapes showed early signs of decay between days 4 and 5, escalating to substantial rotting rates of 20% and 15%, respectively, by the end of the observation period. In stark contrast, the nanocomposite coatings significantly delayed the onset of spoilage; notably, the Grape3, Grape4, and Grape5 samples completely suppressed visible rotting until day 8. By day 9, Grape5 exhibited exceptional protective performance, capping the rotting rate at a minimal 5%, which correlates perfectly with the robust *in vitro* antibacterial data driven by the continuous release of Ag^+ ions. Ultimately, these physiological findings verify that the CS + TiAg1PE formulation functions as a highly effective active packaging material by synergistically coupling the physical barrier properties of the chitosan matrix with the potent antimicrobial action of the silver nanoparticles to significantly extend the shelf life of fresh produce. While the individual components such as CS and TiO_2 (E171) are widely used in various industries, the safety and migration behaviour of the incorporated AgNPs require further systematic evaluation according to national food safety standards. Therefore, the current study focuses on the functional performance of the coating in mitigating decay and weight loss. Future investigations will focus on the biocompatibility and toxicological profiles to ensure the safe implementation of these active coatings in the food industry.

Table 4 presents a comparison of the synthesis route, photocatalytic efficiency, antibacterial activity, and preservative application of the TiAg0.33PE nanocomposite with recently reported TiO_2/Ag-based materials. As summarized in Table 4, while several studies rely on relatively high noble metal loadings (ranging from 10% to 34.3%)[19,37,40,41] or energy-intensive hydrothermal processes,[19,34] the present study achieves remarkable functional outcomes utilizing an ultralow Ag content (0.99%) *via* a completely green, synergistic synthesis route. In terms of environmental remediation, the TiAg0.33PE nanocomposite demonstrates an outstanding photocatalytic efficiency, achieving 95% mineralization of a highly concentrated and recalcitrant RGB dye (30 ppm) within 120 minutes of contact. In contrast, most existing literature predominantly evaluates photocatalytic performance using easily degradable dyes (such as methylene blue or Rhodamine B) at significantly lower concentrations (*e.g.*, 0.03 to 30 ppm).[19,37,40,41] More importantly, while previous research restricts its scope to single-target wastewater treatment or basic *in vitro* antibacterial assays, our study successfully transcends these boundaries. The

Table 4 Comparison of the synthesis route, photocatalytic efficiency, antibacterial activity and preservative application of the TiAg*x*PE nanocomposite with recently reported TiO_2/Ag-based materials[a]

Material	Synthesis method	Metal loading	Photocatalytic performance	Antibacterial activity	Preservation application	Ref.
Ag@TiO_2	Green synthesis (hydrothermal with *Achyranthes aspera* leaf extract + calcinated at 300 °C)	High (11.6%-EDX)	89.96% degradation of methylene blue dye (~3.2 ppm) in 60 min of UV irradiation (0.1 mg mL^{-1} of catalyst dose)	NE	NE	19
TiO_2/Ag	Photodeposition + annealed at 400 °C	High (26.37%-EDX)	98.7% degradation of methylene blue dye (30 ppm) in 50 min of UV irradiation (4 mg mL^{-1} of catalyst dose)	NE	NE	37
Ag/TiO_2	Photoreduction process	High (23.6–34.3%-EDX)	98% degradation of Rhodamine B (20 ppm) in 300 min of visible light (0.6 mg mL^{-1} of catalyst dose)	NE	NE	40
Ag–TiO_2	Sol–gel + calcined at 500 °C	High (10%)	97% degradation of methylene blue dye (0.03 ppm) in 35 min of UV irradiation (1 mg mL^{-1} of catalyst dose)	NE	NE	41
Ag–TiO_2	Green synthesis (sol–gel + hydrothermal + orange peel extract + calcinated at 450 °C)	Medium (3%)	NE	Excellent (*S. aureus*, *L. fermentum*, *S. enterica*, *E. coli*, *P. aeruginosa*)	Mango preservation (chitosan-cyclodextrin matrix, reducing weight loss (14.5%) over 15 days)	34
Ag/TiO_2	Sol–gel + calcinated at 600 °C	Medium (~4.25%)	NE	Excellent (*E. coli*)	Chili and banana preservation (chitosan matrix, reducing weight loss (26.13–53.04%) over 7–10 days)	42
TiO_2/Ag-NPs and gelatin/TiO_2/Ag-NPs	UV deposition	NE	NE	Excellent (*A. fumigatus N1*, *B. spectabilis N2*, *C. xanthochromaticum SPN*, *S. albidoflavus SP11*)	NE	43
TiAg0.33PE	Green synthesis (sol–gel + *Eucalyptus globulus* L. extract + PVA + calcinated at 500 °C)	Ultralow (0.99%-EDX)	92.67% degradation of RGB dye (30 ppm) in 120 min of visible light (0.3 mg mL^{-1} of catalyst dose)	Excellent (*E. coli*, *S. aureus*, *B. cereus*, *P. stutzeri B27*)	Grape preservation (chitosan matrix, reducing weight loss (15%) and rotting (5%) over 9 days)	This study

[a] NE: Not evaluated.

integration of TiAg0.33PE nanocomposite into a biopolymer matrix provides a highly effective active protective coating for real-world grape preservation. Some authors reported using TiO_2/Ag with higher content of Ag[34,42,43] in polymer matrix (chitosan, gelatin, chitosan-cyclodextrin) can help to improve the antibacterial activity of polymer matrix and prolong fruit preservation time. This dual-functional capability substantiates the exceptional potential, cost-effectiveness, and sustainable value of the proposed multipurpose nanomaterial.

4. Conclusion

In summary, highly stable TiAg*x*PE nanocomposites were successfully synthesized and incorporated into a chitosan matrix to fabricate multifunctional active packaging films. Morphological and elemental analyses validated the uniform dispersion of trace AgNPs on a highly porous TiO_2 framework, forming a robust heterojunction. The incorporation of AgNPs to TiO_2 anatase acts as electron traps, capturing conduction band electrons and limiting the electron–hole pairs recombination process. The slight increase in average crystallite size and reduction in the charge transfer resistance of TiAg0.33PE nanocomposite as compared to TiPE nanocomposite confirms that the introduction of Ag not only mitigates charge carrier recombination but also improves electrical conductivity and interfacial charge transfer. The presence of AgNPs in TiAg0.33PE nanocomposite caused a LSPR effect but the intrinsic E_g values of the anatase phase are not drastically altered. This heterojunction structure established an exceptional electron sink that extended the lifespan of charge carriers, thereby achieving rapid and near-complete photocatalytic mineralization of RGB dye. Upon integration into the CS matrix, the inorganic nanoparticles structurally modified the films; while the physical inclusion compromised tensile strength and elongation, it beneficially created a tortuous path that improved the overall moisture barrier performance. The sustained release of Ag^+ ions from the nanocomposites endowed the films with potent bactericidal efficacy against *E. coli* and diverse spoilage pathogens. The application on fresh grapes definitely demonstrated that the CS + TiAg1PE formulation forms a continuous, particle-reinforced protective epidermal layer. This active protective coating effectively mitigates moisture transpiration and microbial decay, capping weight loss at 15% and the rotting rate at 5% after 9 days of storage. Ultimately, this study validates the versatile applicability of the formulated nanocomposites, presenting a sustainable and effective approach for both organic dye degradation and the postharvest shelf-life extension of fresh produce.

Author contributions

Ngoc Linh Nguyen: investigation, writing—original draft. Hoang Thai: writing—reviewing and editing. Thi Thuy Dung Nguyen: investigation, data curation. Tran Dung Hoang: methodology. Dang Hoang Nguyen: investigation. Thuy Chinh Nguyen: conceptualization, funding acquisition, writing—original draft, formal analysis, supervision, data curation, resources, visualization.

Conflicts of interest

The authors declare no competing interests.

Data availability

The datasets used and/or analyzed during the current study are included in the article.

Acknowledgements

This research is funded by Vietnam National Foundation for Science and Technology Development (NAFOSTED) under grant number NCUD.02-2024.12.

References

1 V. Uthiravel, K. Narayanamurthi, V. Raja, S. Anandhabasker and K. Kuppusamy, Green synthesis and characterization of TiO_2 and Ag-doped TiO_2 nanoparticles for photocatalytic and antimicrobial applications, *Inorg. Chem. Commun.*, 2024, **170**(3), 113327, DOI: 10.1016/j.inoche.2024.113327.

2 V. Jadhav, M. Patil, S. Pardeshi, H. Suryavanshi and A. Bhagare, Green synthesis of Ag@TiO_2 nanomaterials using *Achyranthes aspera* leaf extract for sustainable photocatalytic degradation of dyes, *Discover Appl. Sci.*, 2025, **7**, 732, DOI: 10.1007/s42452-025-07324-3.

3 K. M. Elattar, N. M. Askar, N. H. Elhusseini, D. A. Omar, A. S. Ashry, M. M. Keshk, T. R. Saad, A. M. Elzeghiby, A. H. Elnakadi, M. Y. Aboelfatoh and M. Abdelaal, Green Synthesis of Ag/TiO_2 and Ag/Co/TiO_2 Nanocomposites from *Ceratonia siliqua* Extract for Antioxidant and Antibacterial Applications, *ChemistrySelect*, 2025, **10**(38), e03394, DOI: 10.1002/slct.202503394.

4 V. Helen Rathi, A. Rejo Jeice and K. Jayakumar, Green synthesis of Ag/CuO and Ag/TiO_2 nanoparticles for enhanced photocatalytic dye degradation, antibacterial, and antifungal properties, *Appl. Surf. Sci. Adv.*, 2023, **18**, 100476, DOI: 10.1016/j.apsadv.2023.100476.

5 C. Vanlalveni, S. Lallianrawna, A. Biswas, M. Selvaraj, B. Changmai and S. L. Rokhum, Green synthesis of silver nanoparticles using plant extracts and their antimicrobial activities: a review of recent literature, *RSC Adv.*, 2021, **11**, 2804–2837, DOI: 10.1039/D0RA09941D.

6 W. Moges and Y. Misskire, Green synthesis, characterization and antibacterial activities of silver nanoparticles using *Sida schimperiana* Hochst. ex A. Rich (Chifrig) leaves extract, *Discov. Mater.*, 2025, **5**, 34, DOI: 10.1007/s43939-025-00221-x.

7 A. Y. Shala, Mayank Anand Gururani, Phytochemical Properties and Diverse Beneficial Roles of *Eucalyptus globulus* Labill.: A Review, *Horticulturae*, 2021, **7**(11), 450, DOI: 10.3390/horticulturae7110450.

8 G. Tailor and A. M. Lawal, Phytochemical screening; green synthesis, characterization and biological significance of

lead oxide nanoparticles from *Eucalyptus globulus* Labill. (leaves), *Nanotechnol. Environ. Eng.*, 2021, **6**, 48, DOI: 10.1007/s41204-021-00143-y.

9 M. Bello, B. Jiddah-kazeem, T. H. Fatoki, E. O. Ibukun and A. C. Akinmoladun, Antioxidant property of *Eucalyptus globulus* Labill. Extracts and inhibitory activities on carbohydrate metabolizing enzymes related to type-2 diabetes, *Biocatal. Agric. Biotechnol.*, 2021, **36**, 102111, DOI: 10.1016/j.bcab.2021.102111.

10 L. Boulekbache-Makhlouf, E. Meudec, J.-P. Mazauric, K. Madani and V. Cheynier, Qualitative and Semi-quantitative Analysis of Phenolics in *Eucalyptus globulus* Leaves by High-performance Liquid Chromatography Coupled with Diode Array Detection and Electrospray Ionisation Mass Spectrometry, *Phytochem. Anal.*, 2013, **24**(2), 162–170, DOI: 10.1002/pca.2396.

11 W. Liu, Z. Zhang, X. Chen, Y. Mu, D. Zheng, X. Huang, H. Ma and L. Li, Chemical Profiles and Biological Effects of Polyphenols in *Eucalyptus* Genus: A Comprehensive Review on Their Applications in Human Health and the Food Industry, *J. Agric. Food Chem.*, 2025, **73**(17), 10036–10051, DOI: 10.1021/acs.jafc.4c13084.

12 A. Balčiūnaitienė, M. Liaudanskas, V. Puzerytė, J. Viškelis, V. Janulis, P. Viškelis, E. Griškonis and V. Jankauskaitė, *Eucalyptus globulus* and *Salvia officinalis* Extracts Mediated Green Synthesis of Silver Nanoparticles and Their Application as an Antioxidant and Antimicrobial Agent, *Plants*, 2022, **11**(8), 1085, DOI: 10.3390/plants11081085.

13 G. Velmurugan, J. S. Chohan, K. V. Suresh, P. Paramasivam, S. V. Siva and R. Maranan, Green synthesis of silver nanoparticles from southern *Eucalyptus globulus*: Potent antioxidants and photocatalysts for rhodamine B dye degradation, *Desalination Water Treat.*, 2024, **320**, 100687, DOI: 10.1016/j.dwt.2024.100687.

14 V. Rocha, P. Ferreira-Santos, Z. Genisheva, E. Coelho, I. C. Neves and T. Tavares, Environmental remediation promoted by silver nanoparticles biosynthesized by eucalyptus leaves extract, *J. Water Proc. Eng.*, 2023, **56**, 104431, DOI: 10.1016/j.jwpe.2023.104431.

15 G. K. Abere, W. N. Omwoyo, A. M. Osano, J. J. Owuor and E. Suter, Phytochemical-Assisted Synthesis of Silver Nanoparticles Using Eucalyptus Leaf Extract: Structural Characterization and Antimicrobial Evaluation, *Asian J. Phys. Chem. Sci.*, 2025, **13**(4), 36–50, DOI: 10.9734/ajopacs/2025/v13i4262.

16 A. Sahraoui, M. Hamlaoui, S. Chikhi, S. Harrat, O. Baghriche, A. Zertal and S. Vernuccio, Green synthesis and characterization of titanium dioxide nanoparticles using *Eucalyptus globulus* leaf extract: Impacts of the mild thermal treatment, *Mater. Today Sustainability*, 2025, **31**, 101193, DOI: 10.1016/j.mtsust.2025.101193.

17 D. Kanakaraju, F. D. anak Kutiang, Y. C. Lim and P. S. Goh, Recent progress of Ag/TiO_2 photocatalyst for wastewater treatment: Doping, co-doping, and green materials functionalization, *Appl. Mater. Today*, 2022, **27**, 101500, DOI: 10.1016/j.apmt.2022.101500.

18 C. Zarzzeka, J. Goldoni, J. d. R. de Paula de Oliveira, G. G. Lenzi, M. D. Bagatini and L. M. S. Colpini, Photocatalytic action of Ag/TiO_2 nanoparticles to emerging pollutants degradation: A comprehensive review, *Sustainable Chem. Environ.*, 2024, **8**, 100177, DOI: 10.1016/j.scenv.2024.100177.

19 V. Jadhav, M. Patil, S. Pardeshi, H. Suryavanshi and A. Bhagare, Green synthesis of Ag@TiO_2 nanomaterials using *Achyranthes aspera* leaf extract for sustainable photocatalytic degradation of dyes, *Discover Appl. Sci.*, 2025, **7**, 732, DOI: 10.1007/s42452-025-07324-3.

20 K. Agalya, S. Vijayakumar, E. Vidhya, S. Prathipkumar, R. Mythili, S. Devanesan, M. S. AlSalhi and W. Kim, Fabrication of PVA/TiO_2 Composites Via Green Synthesis and Assessment of their Photodegradation and Anti-Germ Capabilities, *Waste Biomass Valor.*, 2024, **15**, 6441–6451, DOI: 10.1007/s12649-024-02507-2.

21 P. Barciela, A. Perez-Vazquez and M. A. Prieto, Azo dyes in the food industry: Features, classification, toxicity, alternatives, and regulation, *Food Chem. Toxicol.*, 2023, **178**, 113935, DOI: 10.1016/j.fct.2023.113935.

22 M. Köktürk, F. Altindağ, G. Ozhan, M. H. Çalimli and M. S. Nas, Textile dyes Maxilon blue 5G and Reactive blue 203 induce acute toxicity and DNA damage during embryonic development of Danio rerio, *Comp. Biochem. Physiol., Part C:Pharmacol., Toxicol. Endocrinol.*, 2021, **242**, 108947, DOI: 10.1016/j.cbpc.2020.108947.

23 M. Abdu, S. Babaee, A. Worku, P. Diale, T. A. M. Msagati and J. F. Nure, Synthesis and optimization of TiO_2-biochar composite for degradation of Basic Blue 41 dye in textile wastewater using response surface methodology, *Inorg. Chem. Commun.*, 2025, **174**(2), 114078, DOI: 10.1016/j.inoche.2025.114078.

24 F. Puga, J. A. Navío and M. C. Hidalgo, A critical view about use of scavengers for reactive species in heterogeneous photocatalysis, *Appl. Catal., A*, 2024, **685**, 119879, DOI: 10.1016/j.apcata.2024.119879.

25 G. Wang, S. Zhang, H. Lu, C. Lu, M. Yang, K. Tang and A. Tang, Montmorillonite helps BiOCl photodegradation of antibiotics, *Environ. Sci.: Nano*, 2023, **10**, 3423–3438, DOI: 10.1039/D3EN00582H.

26 T. H. P. Nguyen, A. Koga, F. N. Nkede, F. Tanaka and F. Tanaka, Application of edible coatings composed of chitosan and tea seed oil for quality improvement of strawberries and visualization of internal structure changes using X-ray computed tomography, *Prog. Org. Coat.*, 2023, **183**, 107730, DOI: 10.1016/j.porgcoat.2023.107730.

27 Li Dong, Development and evaluation of titanium dioxide/chitosan nanocomposite coatings for enhanced food preservation and nutrient retention, *Alex. Eng. J.*, 2025, **121**, 484–491, DOI: 10.1016/j.aej.2025.02.091.

28 L. Dai, X. Wang, J. Zhang and C. Li, Application of Chitosan and Its Derivatives in Postharvest Coating Preservation of Fruits, *Foods*, 2025, **14**(8), 1318, DOI: 10.3390/foods14081318.

29 S. E. A. Hameed, W. M. A. El-Maaty, E. A. Gomaa and F. S. Awad, Redox properties of quercetin iron Ii complex with enhanced antioxidant and antiviral activities, *Sci. Rep.*, 2025, **15**, 44139, DOI: 10.1038/s41598-025-31433-z.

30 N. Aziz, H. Panezai, J. Sun, N. S. Shah, R. Ullah, R. Xu and Z. Jogezai, Degradation of CV dye by the as-synthesized Fe^0–TiO_2 supported clinoptilolite under UV and solar irradiations, *Mater. Adv.*, 2025, **6**, 9179–9195, DOI: 10.1039/D5MA00658A.

31 A. Naeem, M. Javed, A. K. Ayaz, M. Asad, N. Ahmed, Y. M. Raja, N. K. Said, M. A. S. Abdul, M. A. S. M. Haniff and A. Shah, Zircon-Type $CaCrO_4$ Chromite Nanoparticles: Synthesis, Characterization, and Photocatalytic Application for Sunlight-Induced Degradation of Rhodamine B, *ACS Omega*, 2023, **8**(33), 30095–30108, DOI: 10.1021/acsomega.3c02457.

32 V. Kumar, N. Pandey, S. Dharmadhikari and P. Ghosh, Degradation of mixed dye via heterogeneous Fenton process: Studies of calcination, toxicity evaluation, and kinetics, *Water Environ. Res.*, 2020, **92**(2), 211–221, DOI: 10.1002/wer.1192.

33 E. M. Huseynov and E. A. Huseynova, Infrared spectroscopy of nanocrystalline anatase (TiO_2) particles under the neutron irradiation, *Opt. Mater.*, 2023, **144**, 114351, DOI: 10.1016/j.optmat.2023.114351.

34 T. L. Pham, T. M. Huyen Phan, M. B. Nguyen, T. K. Chinh Tran, T. My Hanh Le, V. C. Bui, X. M. Vu, H. V. Doan, T.-T.-B. Nguyen, T. M. Nguyet Hoang and D. L. Tran, Green-synthesized Ag-TiO_2/chitosan-cyclodextrin films for enhanced antibacterial activity and prolonged mango preservation, *Food Biosci.*, 2025, **68**, 106679, DOI: 10.1016/j.fbio.2025.106679.

35 R. Ratshiedana, M. E. Malefane, O. J. Fakayode, G. K. More, A. K. Mishra and A. T. Kuvarega, Ag induced plasmonic TiO_2 for photocatalytic degradation of pharmaceutical under visible light: Insights into mechanism, antimicrobial and cytotoxicity studies, *Mater. Today Commun.*, 2024, **41**, 110753, DOI: 10.1016/j.mtcomm.2024.110753.

36 S. Mostafa, Z. Shi, F. Gholami, P. Fatehi, I. Ahmed and A. Soliman, Ag@TiO_2 Nanocomposite as an Efficient Catalyst for Knoevenagel Condensation, *ACS Omega*, 2022, **7**(36), 32393–32400, DOI: 10.1021/acsomega.2c03852.

37 J. R. Noor, F. K. Mohamad Alosfur, H. B. A. Kadhim and L. M. Ahmed, Synthesis of Ag decorated TiO_2 nanoneedles for photocatalytic degradation of methylene blue dye, *Mater. Res. Express*, 2021, **8**(12), 125013, DOI: 10.1088/2053-1591/ac4408.

38 J. Ashfaq, I. A. Channa, A. G. Memon, I. A. Chandio, A. D. Chandio, M. A. Shar, M. S. Alsalhi and S. Devanesan, Enhancement of Thermal and Gas Barrier Properties of Graphene-Based Nanocomposite Films, *ACS Omega*, 2023, **8**(44), 41054–41063, DOI: 10.1021/acsomega.3c02885.

39 J. Jacob, N. Linson, R. Mavelil-Sam, H. J. Maria, L. A. Pothan, S. Thomas, S. Kabdrakhmanova and D. Laroze, Poly(lactic acid)/nanocellulose biocomposites for sustainable food packaging, *Cellulose*, 2024, **31**, 5997–6042, DOI: 10.1007/s10570-024-05975-w.

40 N. H. Abbas, R. Rasuli and P. Nakhostin Panahi, Decorated titanium oxide with Ag nanoparticles as an efficient photocatalyst under visible light: a novel synthesis approach, *Sci. Rep.*, 2025, **15**, 8207, DOI: 10.1038/s41598-025-92864-2.

41 S. Abbad, K. Guergouri, S. Gazaout, S. Djebabra, A. Zertal, R. Barille and M. Zaabat, Effect of silver doping on the photocatalytic activity of TiO_2 nanopowders synthesized by the sol-gel route, *J. Environ. Chem. Eng.*, 2020, **8**(3), 103718, DOI: 10.1016/j.jece.2020.103718.

42 S. K. Singha, S. M. Hoque, H. Das and Md A. Alim, Evaluation of chitosan-Ag/TiO_2 nanocomposite for the enhancement of shelf life of chili and banana fruits, *Heliyon*, 2023, **9**(11), e21752, DOI: 10.1016/j.heliyon.2023.e21752.

43 N. S. Saada, A. M. Youssef, F. M. Helmi, W. N. Wahba and M. S. Abdel-Aziz, Sustainable gelatin bionanocomposite based on multifunctional TiO_2/Ag-NPs for parchment preservation, *Biomass Convers. Biorefinery*, 2025, **15**, 5171–5182, DOI: 10.1007/s13399-023-05241-2.